




RESEARCH ARTICLE | AUGUST 27 2024

# Three-dimensional trajectories of irregular-shaped tunnel lining fragments in the flow environment caused by high-speed trains

Special Collection: [Flow and Civil Structures](#)

Hong He (何洪) ; Wei-Chao Yang (杨伟超); Yi-Kang Liu (刘义康)  ; E. Deng (邓鐸)



*Physics of Fluids* 36, 085193 (2024)

<https://doi.org/10.1063/5.0220408>



## Articles You May Be Interested In

Effects of windbreak types on aerodynamics of high-speed trains traversing from flat ground to semi-cutting and semi-embankment under crosswinds

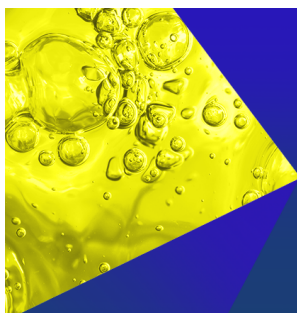
*Physics of Fluids* (July 2024)

A fast three-dimensional flow field prediction around bluff bodies using deep learning

*Physics of Fluids* (February 2024)

Experiment and modeling investigation of irregular block descent into water

*Physics of Fluids* (November 2024)



**Physics of Fluids**  
Special Topics  
Open for Submissions

[Learn More](#)

# Three-dimensional trajectories of irregular-shaped tunnel lining fragments in the flow environment caused by high-speed trains

Cite as: Phys. Fluids **36**, 085193 (2024); doi: [10.1063/5.0220408](https://doi.org/10.1063/5.0220408)

Submitted: 24 May 2024 · Accepted: 17 August 2024 ·

Published Online: 27 August 2024



View Online



Export Citation



CrossMark

Hong He (何洪),<sup>1</sup>  Wei-Chao Yang (杨伟超),<sup>1,2</sup> Yi-Kang Liu (刘义康),<sup>1,a)</sup>  and E. Deng (邓铿)<sup>3,4</sup>

## AFFILIATIONS

<sup>1</sup>School of Civil Engineering, Central South University, Changsha, People's Republic of China

<sup>2</sup>National Engineering Research Center of High-speed Railway Construction Technology, Changsha, People's Republic of China

<sup>3</sup>Department of Civil and Environmental Engineering, The Hong Kong Polytechnic University, Hung Hom, Kowloon, Hong Kong

<sup>4</sup>National Rail Transit Electrification and Automation Engineering Technology Research Center (Hong Kong Branch), The Hong Kong Polytechnic University, Hung Hom, Kowloon, Hong Kong

**Note:** This paper is part of the special topic, Flow and Civil Structures.

<sup>a)</sup>Author to whom correspondence should be addressed: [liuyikang\\_csu@csu.edu.cn](mailto:liuyikang_csu@csu.edu.cn)

## ABSTRACT

High-speed railway tunnel lining fragments can cause collisions with trains and track blockages, severely affecting train operation. When a train passes through a tunnel where lining fragment is likely to occur, the train wind effect may significantly affect the trajectory of the lining fragment, making the location where the lining fragment is difficult to predict. For safety purpose, this study aims to analyze the impact of the initial circumferential position and shape of irregular-shaped lining fragments on their aerodynamic performance. Using on-site scanning and mathematical statistical methods, the shape characteristics and probability distribution of actual lining fragments in the tunnel are obtained. The aerodynamic behavior of irregular-shaped lining fragments with different initial positions and three typical aspect ratios (*AR*s) are investigated based on the overset grid method and the dynamic fluid-body interaction model framework as a high-speed train passes. The study found that the most representative lining fragments with an *AR* of three have a mass of 1.5 kg and are located 2.5 m from the tunnel centerline. The flight behavior of lining fragments shows distinct three-dimensional features, with both translation and rotation significantly affected by the aerodynamic effects of the train and the geometric shape of the fragments. The longitudinal and lateral translational distances of lining fragments at the top of the train decrease as their initial position moves further from the tunnel's centerline. With an increase in *AR*, both the longitudinal and lateral flight distances and average flight velocities of the fragments increase. The macroscopic flow field within the tunnel directly influences the motion characteristics of the lining fragments. Complex flow separation and circulation phenomena near the fragments result in uneven pressure differences acting on the smooth and rough surfaces of the lining fragments, causing irregular motion. The conclusions of this study provide a theoretical basis for assessing and preventing the impact of lining fragments on the operational safety of trains.

Published under an exclusive license by AIP Publishing. <https://doi.org/10.1063/5.0220408>

## NOMENCLATURE

### Abbreviation

$A_p$	largest cross-sectional area perpendicular to $L_{max}$ , m <sup>2</sup>
<i>AR</i>	aspect ratio of lining fragment
$C_{Fi}$	aerodynamic force coefficients
$C_p$	pressure coefficient

$C_w$	empirical constant
$D$	distance between the scanner and the hole, m
$d_w$	distance from the wall, m
$f_{dt}$	delay function associated with DDES
$f_e, f_{hyb}$	enhancement and mixing functions
$f_{step}$	function that facilitates a rapid transition from RANS to LES within the boundary layer
$F_x, F_y, F_z$	force of lining fragment, N
$H$	height of the head train, m

$h_{\max}$	maximum local grid spacing, m
$I$	impulse of lining fragment, N s
$k$	number of circumferential computational unit surfaces within a single segment
$k$	turbulent kinetic energy, J
$L$	length of the head train, m
$L_{\max}$	longest dimension on the smooth surface of lining fragment, m
L1–L5	position of the lining fragment
$L_2$	second longest dimension on the smooth surface perpendicular to $L_{\max}$ , m
$L_3$	longest dimension in the normal direction to the smooth surface, m
$M_x, M_y, M_z$	moment of lining fragment, N m
$m$	mass of lining fragment, kg
$n$	number of longitudinal computational segments along the lining fragment
$\mathbf{n}_{i,j}$	unit normal vector of the computational unit surface at position
$p_{i,j}$	transient surface average pressure exerted on the unit surface at $(i, j)$ , Pa
$P_{\text{inlet}}, P_{\text{outlet}}$	preset pressure value at the inlet and outlet, Pa
$R$	average radius of the cross-sectional area $A_p$ , m
$r$	Pearson's correlation coefficients
$\mathbf{r}_{i,j}$	lever arm vector corresponding to the computational unit surface at $(i, j)$
$\mathbf{S}, \Omega$	normalized strain rate and vorticity tensors
$S_{i,j}$	area of the computational unit surface at $(i, j)$ , $\text{m}^2$
$T'$	non-dimensional time
$t$	falling time of the lining fragment, s
$U_{\text{inlet}}$	velocity component of the fluid in the flow direction, m/s
$\vec{u}$	fluid velocity, m/s
$v_i$	velocity of lining fragment, m/s
$V'_x, V'_y, \text{ and } V'_z$	non-dimensional velocity of the lining fragment
$W$	width of the head train, m
$X_i, Y_i$	sample values of the two variables
$x_i$	displacement of lining fragment, m
$x_i$	distance between point $O_i$ and the origin $O$ , m
$X', Y', \text{ and } Z'$	non-dimensional displacement of the lining fragment
$\bar{X}, \bar{Y}$	sample mean value of the two variables
$\mathbf{y}, \mathbf{z}$	unit vectors in the $Y$ and $Z$ directions
$\partial\Omega_{\text{solid}}$	solid surface boundary
$\vec{n}$	outward normal vector to the inlet boundary
$\partial\Omega_{\text{inlet}}, \partial\Omega_{\text{outlet}}$	inlet and outlet boundary
$\omega$	specific dissipation rate of turbulence, $\text{W}/\text{m}^3$
$\Delta$	subgrid length scale, m
$\nu_t$	eddy viscosity, Pa s
$\kappa$	von Kármán's constant
$\omega_i$	angular velocity of lining fragment, $^\circ/\text{s}$
$\theta_i$	rotation angle of lining fragment, $^\circ$

## I. INTRODUCTION

With the prolonged operation of high-speed railway tunnels, internal diseases such as water leakage, cracking, bottom bulging, and

settlement have gradually emerged, posing a severe threat to the structural integrity and durability of the tunnels.<sup>1–4</sup> Particularly, the aerodynamic pressures and airflow effects generated when trains pass through tunnels at high speeds have a highly detrimental impact on the lining structures, leading to localized detachment of lining materials, a problem that is particularly pronounced in high-speed railway tunnels. The detachment of lining fragments not only diminishes the structural integrity and durability of the tunnels but may also trigger issues such as train collisions and track obstructions, thereby causing damage to trains or injuries to passengers and severely affecting the normal operation of trains. For instance, the lining detachment incident in the Fukuoka Tunnel, Japan, in 1999, and the subsequent train derailment caused by lining detachment in the Rebunhama high-speed railway tunnel in Hokkaido, Japan, in the same year, both resulted in prolonged interruptions to train operations.<sup>5</sup> Additionally, the lining detachment incident at the vault of the Ping Shan Tunnel in China in 2016 also led to a speed reduction for over 2 h, severely affecting the normal operation of trains.<sup>6</sup>

A large number of scholars have conducted in-depth research on the aerodynamic behavior of fragment in wind fields through theoretical research, experimental research, and numerical simulation. Early research mainly focused on the motion characteristics of regular-shaped debris in a constant wind field. For example, as early as 2004, scholars used theoretical research methods to explore the flight trajectory of spherical debris in a one-dimensional (1D) constant wind field, finding that vertical air resistance plays a crucial role in predicting the horizontal and vertical speeds and displacements of debris.<sup>7</sup> In addition, through wind tunnel experiments, researchers have also studied the motion characteristics of plate-like fragment in wind fields, proposed aerodynamic data, and derived empirical formulas for calculating the horizontal movement speed and distance of debris.<sup>8</sup> With the deepening of research, scholars have begun to pay attention to the impact of the turbulence characteristics of the wind field and the randomness of the shape of fragment on aerodynamic behavior. Research has gradually shifted its focus to factors such as the size of debris,<sup>9</sup> the shape coefficient,<sup>10</sup> and the turbulence intensity of the incoming wind.<sup>11,12</sup> With the advancement of computer technology, numerical simulation methods have also been widely applied in this field.<sup>13,14</sup> For instance, Xu *et al.*<sup>15</sup> established a gas–solid coupling model to study the coupled motion characteristics of plate-like wind-borne fragment, taking into account the two-way fluid–solid interaction between fragment and wind field. Saini and Shafei<sup>16</sup> established a coupled computational fluid dynamics and rigid body dynamics (CFD-RBD) simulation framework for simulating the motion trajectory of rod-like debris objects.

Specifically, tornadoes, as a typical turbulent wind field, are also one of the natural phenomena that are more likely to trigger wind-borne fragment. Scholars have generated non-steady flow fields of tornadoes and analyzed the flight trajectories of fragment within these fields.<sup>17,18</sup> Baker and Sterling<sup>19</sup> proposed a conceptual design framework to describe the main characteristics of tornadoes and to generate numerous tornado wind fields and pressure fields, thereby studying the motion trajectories of fragment in tornado wind fields. Maruyama<sup>20</sup> developed a numerical tornado simulator based on large eddy simulation (LES), generating non-steady flow fields of tornado-like vortices, and conducted research on the motion trajectories of fragment, obtaining the statistical distribution of the maximum

horizontal velocity of fragment. Liu *et al.*<sup>21</sup> systematically analyzed the instantaneous distribution, density, and velocity of fragment in tornado wind fields, finding that the maximum difference in velocity between fragment and wind occurs in the core area of the tornado.

The complex aerodynamic effects produced by high-speed train operation exert a significant force on surrounding objects or passengers. For example, the flow field under the train can cause irregular movement of debris under the train, has a significant impact on the movement and accumulation of snow on the track, and has a suction effect on passengers near the track, affecting the safety of people.<sup>22–24</sup> Considering the susceptibility of tunnel lining fragment, the aerodynamic behavior of lining fragment under the more complex train slipstream in the tunnel has also attracted the attention of a few scholars. Shi *et al.*<sup>25</sup> established a three-dimensional (3D) train–tunnel–air–lining fragment coupled computational model, simulating the trajectory characteristics of regular square and circular flake lining fragment when high-speed trains operate at a speed of 300 km/h. In addition, the team also discussed the motion trajectory and force differences of lining fragment under different spalling times based on the improved delayed detached-eddy simulation (IDDES) method<sup>26</sup> and verified the correctness of this method through moving model experiments.<sup>27</sup>

Existing studies have predominantly focused on the aerodynamic behavior of lining fragments with regular shapes, such as squares and circles. However, numerous news reports suggest that the actual lining fragments found at accident sites exhibit irregular shapes.<sup>5,6</sup> Utilizing regular shapes like squares and circles to represent the original complex forms of lining fragments in research is evidently lacking in rationality.

Therefore, this study initially introduces parameters commonly used in the field of wind-induced debris to describe the shape characteristics of irregular-shaped fragments. Through on-site scanning and mathematical statistical methods, the shape characteristics and probabilistic distribution features of real lining fragments within tunnels are obtained. Based on the scanning results, the aerodynamic behavior of lining fragments with different typical shapes and circumferential positions during flight is analyzed using the improved delayed detached-eddy simulation (IDDES) technique and SST  $k-\omega$  turbulence modeling. Section II of this study introduces the definition and acquisition method of the shape parameters of irregular-shaped lining fragments. Section III provides a detailed description of the numerical simulation method based on the shape characteristics of irregular-shaped lining fragments. Section IV validates the correctness of the numerical simulation method from two aspects: grid independence and experimentation. Section V discusses in detail the aerodynamic behavior of lining fragments during flight under different initial circumferential positions and shapes. Section VI presents the main conclusions of this study.

## II. CHARACTERISTICS OF LINING FRAGMENTS

### A. Definition of shape parameter

Apart from external factors such as train speed and tunnel dimensions, the geometric shape and mass of lining fragments are the two parameters that most significantly influence their aerodynamic performance. This study introduces two commonly used parameters in the field of wind-borne debris to describe the geometric characteristics of the fragments,<sup>10,28</sup> namely, the length ratio  $L_{max}$ :  $L_2$ :  $L_3$  and the aspect ratio ( $AR$ ). As shown in Fig. 1, tunnel lining fragments have two

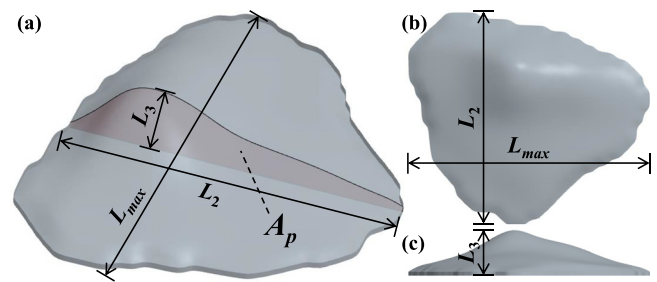


FIG. 1. Definition of shape parameters of the lining fragment: (a) overall schematic; (b) top view; and (c) side view.

characteristic surfaces, the flat surface and the rough surface. The flat surface is the original lining surface.  $L_{max}$ ,  $L_2$ , and  $L_3$  represent the three characteristic lengths of the fragment.  $L_{max}$  is the longest dimension on the flat surface,  $L_2$  is the second longest dimension on the smooth surface perpendicular to  $L_{max}$ , and  $L_3$  is the longest dimension in the normal direction to the flat surface. The definition of the aspect ratio  $AR$  is given in Eq. (1), where  $R$  represents the average radius of the cross-sectional area  $A_p$ , and  $A_p$  is the largest cross-sectional area perpendicular to  $L_{max}$ :

$$AR = \frac{L_{max}}{2\sqrt{A_p/\pi}} = \frac{L_{max}}{2R}. \quad (1)$$

### B. 3D laser scanning method

After the lining fragments detach from the tunnel lining surface, a pit complementary to the shape of the fragment is formed on the originally tunnel lining, as shown in Fig. 2(a). To obtain the geometric shape of actual high-speed railway lining fragments, on-site scanning of pits formed by the detachment of lining fragments is conducted within tunnels along a railway line in China, with a total of 69 pits scanned. It is noteworthy that after the formation of the pit from the lining fragment detachment, the adhesion of the concrete surface of the pit is reduced. Consequently, tunnel management departments typically chisel away the concrete near the pit to prevent further detachment of unstable concrete debris, as shown in Fig. 2(b). The scanning work is only conducted on the undisturbed lining pits. A Leica P50 3D laser scanner is used for the scanning work, which offers the advantages of high precision and long measuring range, supporting scanning at a distance of up to 1000 m with a scanning field of view of

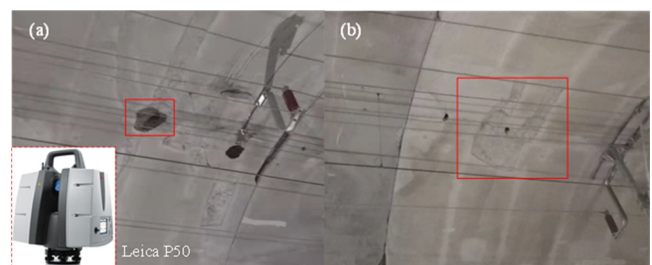


FIG. 2. Field photographs: (a) pit formed by the detachment of the lining fragment and (b) pit after chiseling.



up to  $360^\circ \times 290^\circ$ . Considering that the height of the arch of high-speed railway tunnels in China is typically around 10 m, the scanning distance is set to the minimum allowable value of the instrument at 120 m, with a corresponding scanning rate of  $1 \times 10^6$  points per second. The size of the lining fragments usually ranges from 10 to 100 cm. To more accurately capture the nuances of the tunnel lining's surface, we employed a scanner with high precision capabilities. Specifically, the scanner's horizontal and vertical angular accuracy is  $8''$ , the ranging accuracy is calculated as  $1.2 + 10 \times 10^{-6}D$  (where  $D$  denotes the distance between the scanner and the hole, unit: m), and the accuracy of the point cloud noise is maintained at 0.4 mm. Additionally, the scanner's positioning accuracy is 0.8 mm@10 m.

After the on-site scanning, the three-dimensional point cloud data of the lining detachment pits are imported into CloudCompare to obtain the aspect ratio (AR), the length ratio ( $L_{max}: L_2: L_3$ ), and the volume of the lining fragments. Multiplying the volume of the fragments by the density of the concrete ( $2.4 \text{ g/cm}^3$ ) yields the mass of the lining fragments.

### C. Analysis of scanning results

Considering that concrete inherently possesses a certain degree of cohesion, the AR of lining fragments is not entirely independent of the length ratio ( $L_{max}: L_2: L_3$ ). To conduct a reasonable analysis of influential factors, it is necessary to study the correlation between these three parameters. Analysis of the results obtained from the on-site scanning indicates that the range of the AR for the fragments is between two and seven, and the normalized lengths are between zero and 23. Among these samples, approximately 80% of the lining fragments have an AR value concentrated between two and four, with only a minority of lining fragments having an AR value exceeding four. The universality of the research subjects is crucial for ensuring the broad applicability of the research results; hence, this research focuses on the lining fragments with an AR value within the range of two to four. Consequently, Fig. 3 only presents the relationship between AR and the characteristic length ( $L_{max}: L_2: L_3$ ) of the lining fragments when AR is between two and four. The ordinate values in the figure represent AR, and the abscissa represents the normalized values of  $L_{max}$  and  $L_2$  (i.e.,  $L_{max}: L_3$  and  $L_2: L_3$ ). Furthermore, the Pearson's correlation coefficient is used to evaluate the correlation between them, which is defined by Eq. (2). The calculations show that the Pearson's correlation coefficients all greater than 0.88, indicating that there is a strong positive

correlation between the AR of the fragments and their characteristic lengths.

$$r = \frac{\sum_{i=1}^n (X_i - \bar{X})(Y_i - \bar{Y})}{\sqrt{\sum_{i=1}^n (X_i - \bar{X})^2} \sqrt{\sum_{i=1}^n (Y_i - \bar{Y})^2}}. \quad (2)$$

Figure 4 analyzes the statistical characteristics of the fragment's AR, mass ( $m$ ), and distance between lining fragments and tunnel centerline ( $D$ ). As shown in Fig. 4, when the AR of the lining fragments is between two and four, their mass is primarily distributed between 0.5 and 3 kg, and their distance from the tunnel centerline is mainly within 0–5 m. Samples within these ranges account for approximately 80% of the total. Notably, the most representative lining fragments with an AR of three have a mass of 1.5 kg and are located 2.5 m from the tunnel centerline, with corresponding proportions of 17.6% and 10.8%.

## III. CFD MODEL

### A. Lining fragment modeling

Given that the focus of this research is to investigate the impact of the shape of lining fragments on their aerodynamic performance, it is necessary to select lining fragments with the same mass as the research subjects. Since obtaining lining fragments with completely identical mass from on-site scanning is not realistic, we chose lining fragments with different AR but with nearly the same mass as the research subjects. Based on the results of on-site scanning, Fig. 5 illustrates the three types of lining fragments selected for this study, with AR values of two, three, and four, and masses of 1.48, 1.51, and 1.54 kg, respectively, designated as AR2, AR3, and AR4. These lining fragments form as a result of the detachment of concrete from the lining surface, and their shapes are complementary to the pits on the lining surface. Therefore, to more closely approximate actual conditions, the bottom surfaces of the three shapes of lining fragments established in this study are smooth, while the top surfaces are rough and complementary to the lining pits. To facilitate grid generation, the surfaces of the three fragments undergo a certain degree of smoothing.

### B. Computational domain and boundary conditions

As illustrated in Fig. 6, the train model is based on the widely utilized 8-car CRH 380B high-speed train in China. The presence of

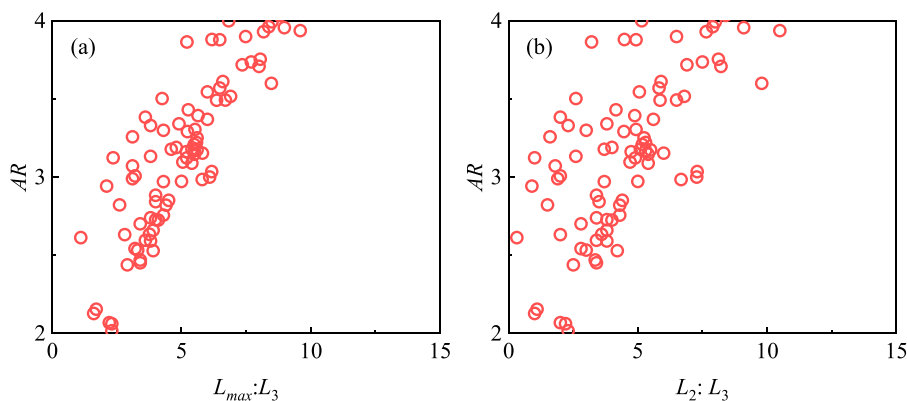
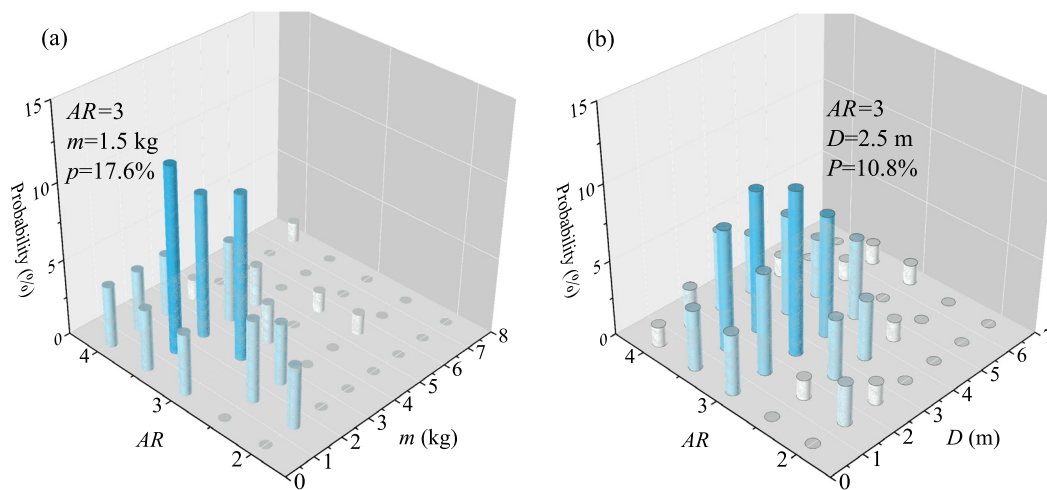
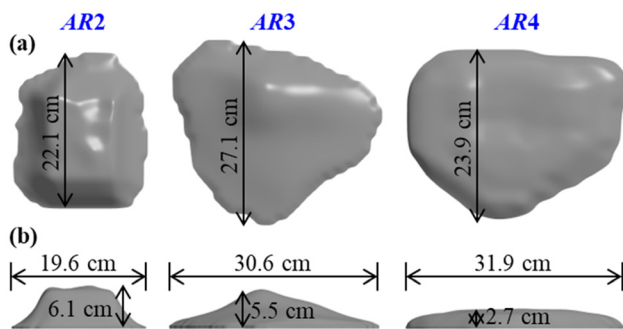


FIG. 3. Correlation analysis: (a) AR and  $L_{max}:L_3$  and (b) AR and  $L_2:L_3$ .



**FIG. 4.** The statistical characteristics between the parameters of the fragment: (a) fragment's AR and mass ( $m$ ) and (b) fragment's AR and distance between lining fragments and tunnel centerline ( $D$ ).



**FIG. 5.** Geometrical shapes and dimensions of lining fragments with different AR: (a) top view and (b) side view.

bogies leads to intricate flow patterns beneath the train, with a notable increase in the velocity of the slipstream.<sup>29–32</sup> Given the possibility that some lining fragments may fall from the sides of the train and be entrained into the bogie area, this research incorporates the influence

of the bogies on the train's surrounding flow field in its computational analysis. The head train's dimensions are  $L$  ( $L = 25.965$  m) in length,  $W$  ( $W = 3.202$  m) in width, and  $H$  ( $H = 3.722$  m) in height, while the lengths of the six intermediate trains are all  $0.96L$ . The computational domain of the numerical model is composed of two atmospheric ends and a tunnel in the middle. The two atmospheric ends are simulated in a semi-cylindrical form, with diameters and heights of 200 and 300 m, respectively. The tunnel dimensions are determined according to the standard specifications of a  $100\text{ m}^2$  single-bore double-track tunnel, with length, width, and height dimensions of 400 m, 12.6, and 9.08 m, respectively. The lining fragments are all placed at the central cross section of the tunnel. The coordinate origin ( $O$ ) is located at the middle position on the bottom surface of the tunnel's central cross section. The positive direction of the  $X$ -axis is aligned with the direction of train operation. The positive direction of the  $Y$ -axis is vertical upward, which is opposite to the direction of the lining fragment's fall. The positive direction of the  $Z$ -axis is the horizontal direction, which follows the right hand-rule.

For solid surfaces such as tunnel wall, ground, train surface, and lining fragment surface, the relative velocity between the fluid and the

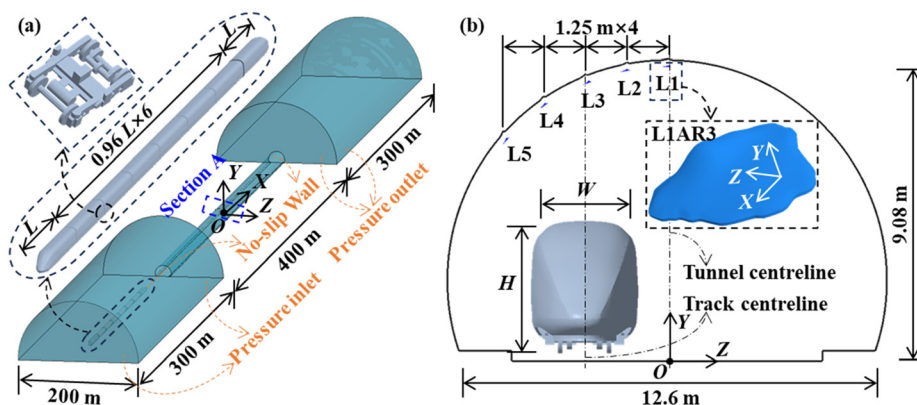


**FIG. 6.** Computational domain: (a) overall model and (b) cross section.

solid surface is zero  $[\vec{u}(x) = 0, \forall x \in \partial\Omega_{solid}]$ , where  $\vec{u}$  represents the fluid velocity and  $\partial\Omega_{solid}$  represents the solid surface boundary]. The boundary condition is set as no-slip Wall. In numerical simulations, since it is impossible to simulate an infinitely large computational domain, we choose a sufficiently large space as the external boundary of the simulation and set the pressure to zero on this boundary to approximate the atmospheric conditions at infinity. For the inlet, the fluid flows into the computational domain from this area  $[p(x) = P_{inlet}, \vec{u}(x) \cdot \vec{n} = U_{inlet}, \forall x \in \partial\Omega_{inlet}]$ , where  $P_{inlet}$  is the preset pressure value at the inlet, set to zero here;  $U_{inlet}$  is the velocity component of the fluid in the flow direction;  $\vec{n}$  is the outward normal vector to the inlet boundary; and  $\partial\Omega_{inlet}$  represents the inlet boundary], the boundary condition is set as pressure inlet. For the outlet, the fluid flows out of the computational domain from this area  $[p(x) = P_{outlet}, \forall x \in \partial\Omega_{outlet}]$ , where  $P_{outlet}$  is the pressure value at the outlet; and  $\partial\Omega_{outlet}$  represents the outlet boundary], the boundary condition is set as pressure outlet.

Through on-site scan, it is found that the lining fragments are mostly distributed within a 5-m range from the tunnel centerline. Furthermore, given that the main objective of this study is to evaluate the impact of lining fragments on the safety of train operation, we pay special attention to the positions that may collide with the train when they fall. Based on the above two aspects, we select five positions of lining fragments that are uniformly distributed in a certain range above the train as the research objects [Fig. 6(b)]. The horizontal distance of 1.25 m between adjacent lining fragments. Positions L1 and L3 are, respectively, defined as points on the tunnel's centerline and the track's centerline where they intersect with the tunnel wall. For ease of description, the fragment at position L1 is referred to as the tunnel centerline fragment, while those at positions L2, L3, and L4 are collectively termed as the top of the train fragments, and the fragment at position L5 is designated as the tunnel sidewall fragment. The nomenclature for each scenario reflects the position and shape of the lining fragment, for example, "L1AR3" denotes a lining fragment with an AR of three that begins to fall from position L1. In addition, considering that the lining fragments at L3 are distributed across the AR range of two to four, we have further investigated the aerodynamic behavior of these fragments when the AR values are specifically two, three, and four at L3. Table I provides details information of all scenarios involved in this study.

To ensure the quality of grid generation near the lining fragments, the vertical distance from the top of the lining fragments to the tunnel wall is uniformly set to 2 cm. Under the initial conditions,

TABLE I. investigated cases.

Number	Case	Location	AR of lining fragments	Train speed (km/h)
1	L1AR3	Tunnel centerline	3	300
2	L2AR3	Top of the train	3	
3	L3AR3	Top of the train	3	
4	L4AR3	Top of the train	3	
5	L5AR3	Tunnel sidewall	3	
6	L3AR2	Top of the train	2	
7	L3AR4	Top of the train	4	

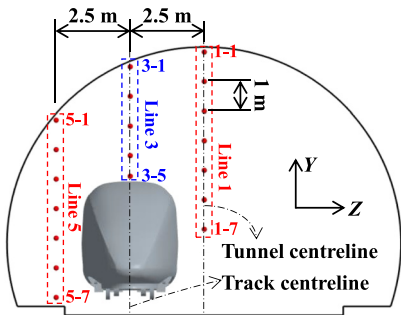


FIG. 7. Location of wind speed virtual probes.

the train's nose is positioned  $2L$  away from the tunnel entrance. When the train's nose is exactly at the middle of the tunnel, the lining fragment falls under the action of gravity and train's surrounding flow. The free motion of the lining fragments is simulated by activating the six degrees of freedom (6 DOF) model in the STAR-CCM+ software, and the dynamic fluid-body interaction (DFBI) framework is employed to capture the dynamic behavior of the lining fragments within the train's surrounding flow field. In all simulations, the train's operating speed is set at 300 km/h. Figure 7 also presents a schematic of the wind speed virtual probes layout, with all virtual probes arranged on the tunnel's central cross section. Specifically, the virtual probes are vertically arranged along positions corresponding to the lining fragments at L1, L3, and L5, starting at the tunnel wall and extending downward at 1 m intervals along the vertical direction.

C. Grid model and solution setting

To ensure both grid quality and computational efficiency, a dynamic overset grid method is employed to simulate the motion of the lining fragments and the train. During the computation, this method achieves precise simulation of complex geometries in motion by cutting a hole within the background grid region and filling the space with an overset grid region. Figure 8 shows the schematic of the grid partitioning strategy, the computational domain is divided into three main regions: The air-filled domain serves as the background region (region 1), which remains stationary throughout the computation. The cuboid containing the train (region 2) and the spherical region of a lining fragment with a radius of  $0.02L$  (region 3) are defined as overset regions, performing linear motion and free fall motion during the computation, respectively. Each region utilizes the STAR-CCM+ software to generate trimmed body grids, a grid type renowned for its high quality and minimal quantity.<sup>33,34</sup> Furthermore, eight layers of boundary layer grids are set up on the surfaces of the train and the bogie, with a growth rate of 1.5 and a total thickness of  $0.01H$ , ensuring that the  $y^+$  values are within the range of 10–20, which guarantees the accuracy of the near-wall treatment. For the lining fragment surface, ten layers of boundary layer grids are set, with a total thickness of  $0.001H$ , to capture the complex aerodynamic interactions. After the meticulous grid partitioning and discretization process described above, the final total grid count is approximately  $57.4 \times 10^6$  cells.



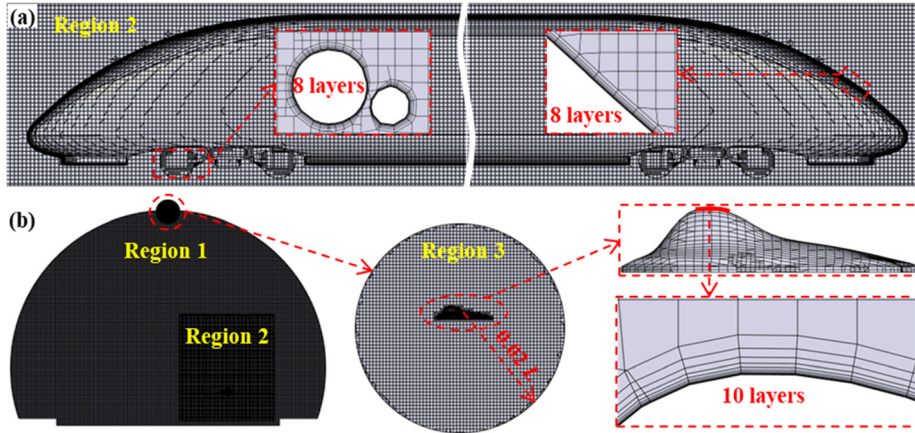


FIG. 8. The schematic of the grid partitioning strategy: (a) longitudinal view of the grid around the train and (b) cross-sectional view of the grid in the central cross section of the tunnel.

In this study, an improved delayed detached eddy simulation (IDDES) combined with the SST  $k-\omega$  turbulence model is utilized to achieve an accurate simulation of the macroscopic flow within the tunnel and the local flow field of the lining fragment.<sup>27,35</sup> The IDDES turbulence model captures the multi-scale characteristics of turbulence by employing the robustness of the high Reynolds averaged Navier-Stokes (RANS) method in the near-wall region, while utilizing the high-resolution features of large eddy simulation (LES) in the free-shear regions away from the wall. This dual-phase treatment strategy not only enhances computational efficiency and reduces the demand for computational resources but also ensures the accuracy and reliability of the simulation results through an intelligent transition from RANS to LES.

The length scales of IDDES are as follows:<sup>36,37</sup>

$$l_{hyb} = f_{hyb}(1 + f_e) \frac{\sqrt{k}}{C_\mu \omega} + (1 - f_{hyb}) C_{DES} \Delta, \quad (3)$$

$$f_{hyb} = \max\{(1 - f_{dt}), f_{step}\}, \quad (4)$$

$$f_{dt} = 1 - \tanh \left[ \left( 20 \frac{\nu_t}{\kappa^2 d_w^2 \sqrt{0.5(S^2 + \Omega^2)}} \right)^3 \right], \quad (5)$$

where  $f_e$  and  $f_{hyb}$  denote the enhancement and mixing functions, respectively;  $\omega$  signifies the specific dissipation rate of turbulence;  $k$  is indicative of the turbulent kinetic energy;  $\Delta$  corresponds to the subgrid length scale;  $f_{dt}$  is the delay function associated with DDES;  $f_{step}$  is a function that facilitates a rapid transition from RANS to LES within the boundary layer;  $\nu_t$  symbolizes the eddy viscosity;  $\kappa$  is the von Kármán's constant;  $d_w$  is the distance from the wall; while  $S$  and  $\Omega$  represent the normalized strain rate and vorticity tensors, respectively, in relation to the turbulence timescale.

Additionally, a new definition of the subgrid length scale is provided in the IDDES model, with the following calculation formula:

$$\Delta = \min\{C_w \max[d_w, h_{\max}], h_{\max}\}, \quad (6)$$

where  $h_{\max}$  represents the maximum local grid spacing, and  $C_w$  is an empirical constant, taken as 0.15.

The discretization of the temporal term is achieved using a second-order implicit method. For the pressure term in the governing

equations, a second-order accurate discretization scheme is employed. The calculation of the momentum terms is based on a bounded central difference scheme. The modified turbulence energy viscosity term is discretized using a second-order upwind scheme. The coupling between pressure and velocity is resolved using the SIMPLE algorithm. With a set time step of  $5 \times 10^{-5}$  s, it is ensured that the Courant number (CFL) for over 99% of the grid is below one, while the maximum CFL value does not exceed 1.3. Within each physical time step, 30 iterations are performed to ensure that the residuals are reduced below  $10^{-6}$ , thereby guaranteeing the convergence of the computation.

#### D. Data processing

During the falling process, the lining fragments are primarily subjected to six aerodynamic loads:  $F_x$ ,  $F_y$ ,  $F_z$ ,  $M_x$ ,  $M_y$ , and  $M_z$ . Among these,  $F_y$  is the force in the direction of gravity, which is less affected by the flow field around the train. Therefore, the focus is on the other five aerodynamic loads. In this research, the pressure integration method is used to calculate the aerodynamic loads on the lining fragments. This method involves dividing the surface of the fragment into multiple calculation segments and integrating the forces applied to each segment to obtain the overall aerodynamic load on the fragment. Figure 9 provides a detailed illustration of the pressure integration method, where  $O$  is the center of gravity of the lining fragment, and  $O_i$  represents the center of gravity of the  $i$ th calculation segment. The corresponding calculation formulas are as follows:

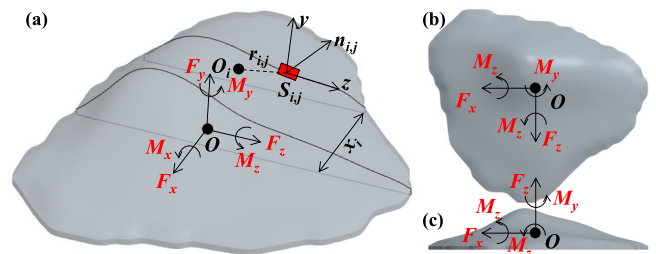


FIG. 9. Schematic diagram of the aerodynamic load calculation plan for lining fragments: (a) overall schematic; (b) top view; and (c) side view.



$$\left\{ \begin{array}{l} F_x = \sum_{i=1}^n \left( \sum_{j=1}^k (p_{i,j} \cdot S_{i,j} \cdot (\mathbf{n}_{i,j} \cdot \mathbf{x})) \right), \\ F_z = \sum_{i=1}^n \left( \sum_{j=1}^k (p_{i,j} \cdot S_{i,j} \cdot (\mathbf{n}_{i,j} \cdot \mathbf{z})) \right), \\ M_x = \sum_{i=1}^n \left( \sum_{j=1}^k (p_{i,j} \cdot S_{i,j} \cdot (\mathbf{r}_{i,j} \times \mathbf{n}_{i,j})) \right), \\ M_y = \sum_{i=1}^n \left( \sum_{j=1}^k (p_{i,j} \cdot S_{i,j} \cdot (\mathbf{n}_{i,j} \cdot \mathbf{z}) \cdot x_i) \right), \\ M_z = \sum_{i=1}^n \left( \sum_{j=1}^k (p_{i,j} \cdot S_{i,j} \cdot (\mathbf{n}_{i,j} \cdot \mathbf{y}) \cdot x_i) \right), \end{array} \right. \quad (7)$$

where  $n$  signifies the number of longitudinal computational segments along the lining fragment;  $k$  denotes the number of circumferential computational unit surfaces within a single segment;  $\mathbf{y}$  and  $\mathbf{z}$  represent the unit vectors in the  $Y$  and  $Z$  directions, respectively;  $\mathbf{n}_{i,j}$  is the unit normal vector of the computational unit surface at position  $S_{i,j}$  denotes the area of the computational unit surface at  $(i, j)$ ;  $p_{i,j}$  is the transient surface average pressure exerted on the unit surface at  $(i, j)$ ;  $x_i$  indicates the distance between point  $O_i$  and the origin  $O$ ; and  $\mathbf{r}_{i,j}$  signifies the lever arm vector corresponding to the computational unit surface at  $(i, j)$ .

During the falling process, the lining fragment undergoes rigid body motion; hence, its motion follows the equations of motion for a rigid body, which are Newton's laws of motion and the conservation of angular momentum. The formulas for calculating its velocity ( $v_i$ ), displacement ( $x_i$ ), angular velocity ( $\omega_i$ ), and rotation angle ( $\theta_i$ ) are as follows:

$$\left\{ \begin{array}{l} v_i = \int_0^t \frac{F_i}{m} dt + v_0, \\ x_i = \int_0^t v_i dt + x_0, \end{array} \right. \quad (8)$$

$$\left\{ \begin{array}{l} \omega_i = \int_0^t \frac{M_i}{I_i} dt + \omega_0, \\ \theta_i = \int_0^t \omega_i dt + \theta_0, \end{array} \right. \quad (9)$$

where:  $i = 1, 2$  and  $3$ , represent the  $x$ ,  $y$ , and  $z$  directions, respectively;  $F_i$  and  $M_i$  represent the instantaneous force and torque on the lining fragment, respectively;  $m$  and  $I$  are the mass and the moment of inertia about the axis of the lining fragment, respectively;  $t$  is the falling time of the lining fragment; and  $v_0$ ,  $x_0$ ,  $\omega_0$ , and  $\theta_0$  are the initial velocity, displacement, angular velocity, and rotation angle of the lining fragment, respectively.

To delve into the regularities of the trajectory and aerodynamic load variations of lining fragments during their flight, this study

employs the non-dimensionalization method described in Eqs. (10)–(14) to render certain physical quantities non-dimensional. These include non-dimensional time ( $T'$ ), non-dimensional displacement ( $X'$ ,  $Y'$ , and  $Z'$ ) and velocity ( $V'_X$ ,  $V'_Y$ , and  $V'_Z$ ) of the lining fragment, as well as parameters such as aerodynamic force coefficients ( $C_{Fi}$ ) and pressure coefficient ( $C_p$ ).

$$T' = tv_t/L, \quad (10)$$

$$X' = x/L, \quad Y' = y/H, \quad Z' = z/W, \quad (11)$$

$$V'_X = V_X/v_t, \quad V'_Y = V_Y/v_t, \quad V'_Z = V_Z/v_t, \quad (12)$$

$$C_{Fi} = \frac{1}{2} \rho v_t^2 A F_i, \quad (13)$$

$$C_p = \frac{P}{0.5 \rho v_t^2}, \quad (14)$$

where  $t$  denotes the physical time, with the moment the lining fragment begins to fall defined as  $t = 0$ ;  $v_t$  represents the train's operating speed;  $x$ ,  $y$ , and  $z$  represent the displacement of the lining fragment in three directions;  $L$ ,  $W$ , and  $H$  denote the length, width, and height of the head train, respectively;  $V_X$ ,  $V_Y$ , and  $V_Z$  represent the velocity of the lining fragment in three directions;  $F_i$  ( $i = x, y$ , and  $z$ ) indicates the aerodynamic forces on the lining fragment;  $\rho$  signifies the air density;  $A$  is the characteristic area of the lining fragment; and  $P$  is the pressure.

## IV. VERIFICATION

### A. Sensitivity test

To avert simulation errors due to improper grid division and enhance the credibility of the numerical simulation results, given the focus of this study on analyzing the aerodynamic behavior of lining fragments, three different densities, named as scheme 1, scheme 2, and scheme 3, of grids are employed for the discretization of the lining fragment surface [as shown in Fig. 10(a)]. The grid density in other regions within the computational domain is correspondingly adjusted based on the grid density around the lining fragment to ensure a rational distribution of the grid across the entire computational domain. Among the three schemes, the total number of grids for scheme 1, scheme 2, and scheme 3 are  $27.3 \times 10^6$ ,  $57.4 \times 10^6$ , and  $110 \times 10^6$ , respectively. The selected case is L3AR3, with all other boundary conditions and solution methods consistent with Sec. III.

Figure 10(b) presents a comparison of the time history curves of the flight velocity of the lining fragment in the  $X$  direction under different grid densities, along with their average values. The analysis results indicate that although there are certain differences among the three schemes during the simulation process, the trend of the flight velocity change of the lining fragment in the  $X$  direction is generally consistent, especially during the first half of the simulation time, where the flight velocities obtained from different schemes are highly congruent. It is noteworthy that under scheme 2 and scheme 3, the numerical simulation results exhibit a high degree of consistency, with the average flight velocities in the  $X$  direction being  $3.37 \times 10^{-3}$  and  $3.47 \times 10^{-3}$ , respectively, resulting in a difference of merely 2.9%. In contrast, the difference between scheme 1 and scheme 2 is larger, reaching 8.4%. The aforementioned results suggest that scheme 2 employed in this study can ensure sufficient computational accuracy while effectively controlling the use of computational resources, achieving an optimal balance between computational efficiency and cost.

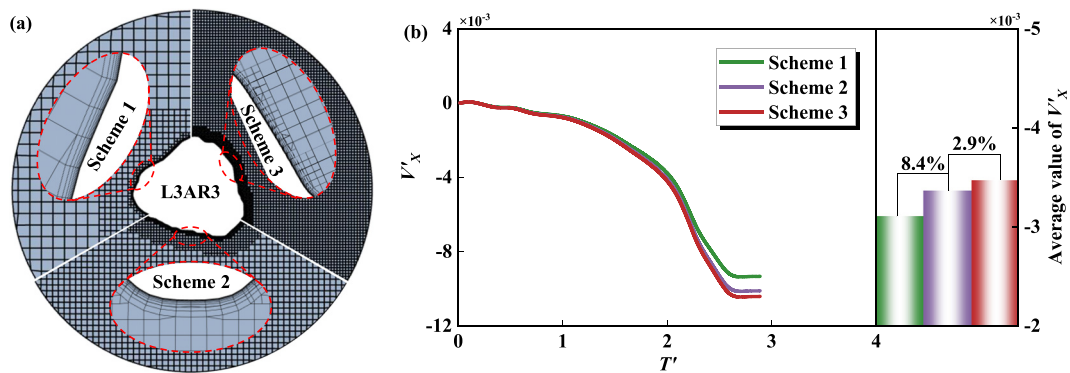


FIG. 10. Grid sensitivity analysis: (a) different density grids and (b) flight velocity in the X direction.

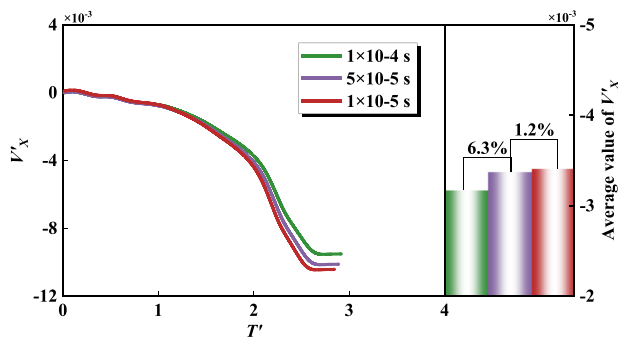


FIG. 11. Time step sensitivity analysis.

This research also carried out a sensitivity analysis on the time step size, selecting three time step sizes:  $1 \times 10^{-4}$ ,  $5 \times 10^{-5}$ , and  $1 \times 10^{-5}$  s. The selected case is L3AR3, with all other boundary conditions and solution methods consistent with Sec. III. Figure 11 displays the velocity time history curves of the lining fragments along the X direction and a comparison of average velocities at these three time step sizes. Upon analysis, the velocity trend of the lining fragments in the X direction is basically consistent under the three different time step sizes, but there are slight differences in the average velocity. Specifically, there is a significant difference in average velocity between the  $1 \times 10^{-5}$  and  $5 \times 10^{-5}$  s schemes, reaching 6.3%, while the difference in average velocity between the  $1 \times 10^{-4}$  and  $5 \times 10^{-5}$  s schemes is 1.2%. These results indicate that choosing a time step size of  $5 \times 10^{-5}$  s can ensure computational accuracy while also ensuring computational efficiency.

## B. Moving model experiment validation

To validate the accuracy of the numerical simulations in this research, a corresponding numerical model is constructed in reference to the moving model experiment conducted by Deng *et al.*<sup>27</sup> In the high-speed moving model experiment, an automatic device for the falling and motion capture of lining fragments was established. The high-speed train was configured in a three-car formation, scaled down by a ratio of 1:20, with consideration given to the impact of the bogies on

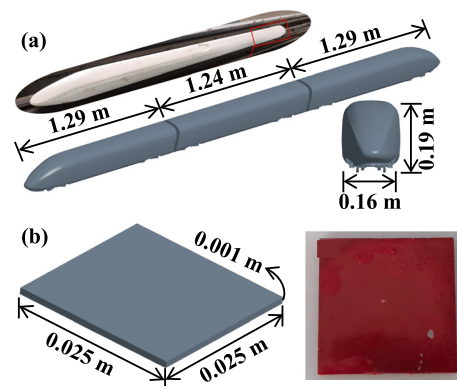


FIG. 12. Experimental and numerical models: (a) train model and (b) lining fragment model.

the flow field structure. Both the head and tail trains measure 1.29 m in length, while the middle train is 1.24 m long, with the width and height of the train cars being 0.16 and 0.19 m, respectively [Fig. 12(a)]. The train speed is set at 350 km/h. The lining fragment is modeled as a regular cuboid with edge lengths of 0.025 m and a thickness of 0.001 m [Fig. 12(b)]. High-speed cameras, capturing at a frame rate of 2000 Hz, were utilized to monitor the longitudinal flight trajectory of the lining debris. The mesh division, boundary conditions, and solution settings are consistent with those detailed in Sec. III.

Figure 13 presents a comparison of the displacement and velocity of the lining fragment in the X direction obtained from the moving model experiment and the numerical simulation. Upon comparative analysis, it is observed that the results from the two methods exhibit a high degree of consistency and share the same trend of variation. The maximum differences in the displacement and velocity of the lining fragment in the X direction are  $-3.21\%$  and  $-3.09\%$ , respectively. The numerical simulation results show a high degree of consistency with the experimental results in the initial phase of the curve. However, differences emerge in the later stages (when  $t' > 5$ ). This is primarily because the falling behavior of the lining fragments in the later period is mainly influenced by the wake vortices, and it is difficult for the numerical simulation to fully replicate the wake vortices observed in

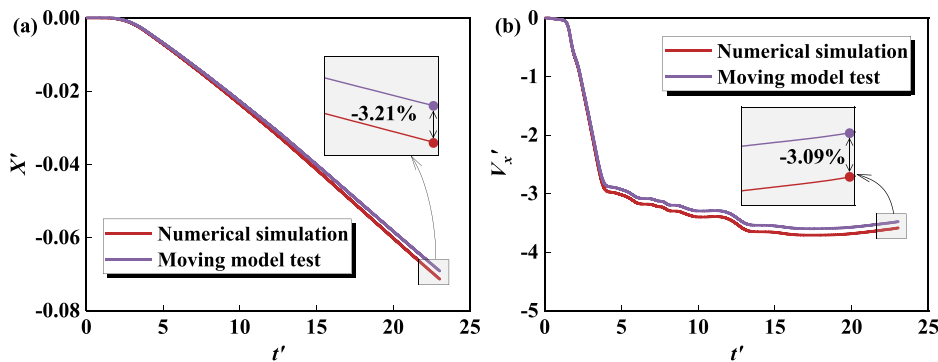


FIG. 13. Comparison of moving model test and simulation results: (a) displacement in  $X$  direction and (b) velocity in  $X$  direction.

the experiment. The complexity of the train's wake vortices leads to discrepancies between the numerical simulation and experimental data in the later motion behavior. Nonetheless, overall analysis indicates that the numerical simulation method employed in this research can effectively simulate the flight trajectory of the lining fragments as they fall within the tunnel, thereby verifying the accuracy of the numerical simulation method.

## V. RESULTS AND DISCUSSION

### A. Flight characteristics of falling debris

#### 1. Falling debris translation

Figure 14 presents the translational trajectories of lining fragments with different initial circumferential positions and various  $AR$  within the  $XY$  plane, while Fig. 15 provides the trajectories within the  $YZ$  plane, with an enlarged view in Fig. 15 highlighting the translational distances of different lining fragments in the  $Z$  direction. As shown in Figs. 14 and 15:

- (1) Under the action of train slipstream, the translational trajectories of lining fragments with different initial circumferential

positions and various  $AR$  exhibit three-dimensional characteristics, with the translational distances in the  $X$  direction significantly exceeding the corresponding values in the  $Z$  direction. In the  $XY$  plane, the flight trajectories of the lining fragments are in the opposite direction to the train's movement; in the  $YZ$  plane, the lining fragments all move in the positive  $Z$  direction. The trajectories of the fragments in the  $XY$  plane are similar in shape to a parabola.

- (2) The translational patterns of fragments dropped from different initial circumferential positions show significant differences. Specifically, neither the L1AR3 nor the L5AR3 fragments come into contact with the train, and their longitudinal movement distances are much greater than those of the other three fragments, with their lateral movement distances also being relatively large. The longitudinal and lateral movement distances of the L5AR3 fragment are 45.3% and 5.2% less than the corresponding values for the L1AR3 fragment, respectively. For the fragments L2AR3, L3AR3, and L4AR3, as the distance between the initial circumferential position of the fragment and the tunnel's centerline increases, the longitudinal and lateral

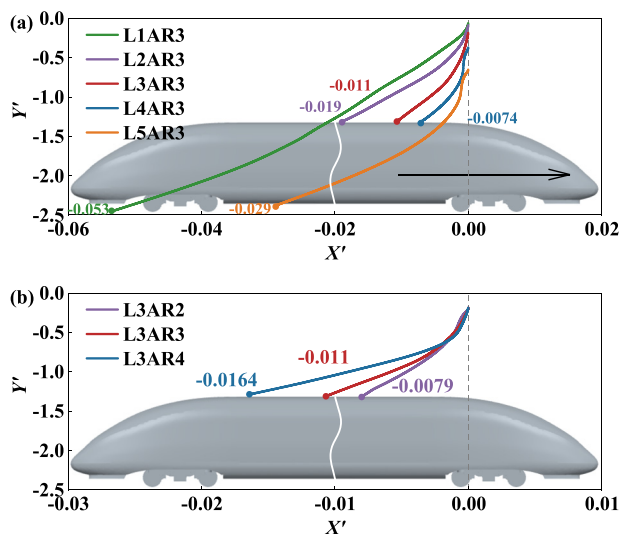


FIG. 14. Translational trajectories in the  $XY$  plane of the lining fragment: (a) different initial circumferential positions and (b) different  $AR$ .

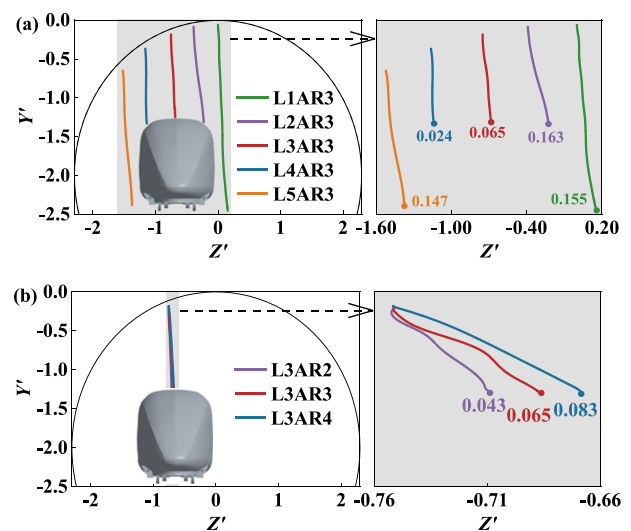


FIG. 15. Translational trajectories in the  $YZ$  plane of the lining fragment: (a) different initial circumferential positions and (b) different  $AR$ .

translational distances for all three decreases. The longitudinal and lateral translational distances of the L4AR3 fragment are only 38.9% and 14.7% of the corresponding values for the L2AR3 fragment, respectively. Although the fragments L2AR3, L3AR3, and L4AR3 exhibit some translation in the Z direction, all three collide with the train's roof, posing a threat to the safety of train operation.

- (3) There is a clear commonality in the translational patterns of fragments with different AR, with differences only in the distances moved. Under the condition of equal total mass, the longitudinal and lateral translational distance of the fragment increases with an increase in AR. When the AR of the fragment increases from two to four, its longitudinal and lateral translational distances increase by 107.6% and 93.0%, respectively.

Figure 16 respectively compares the X and Z direction translational velocities of lining fragments with different initial circumferential positions and various AR. As shown in Fig. 16:

- (1) Under conditions of different initial circumferential positions and various AR, the translational velocity of the lining fragments in the X direction is negative, while the average velocity in the Z direction is positive, with the translational velocity in the X direction being greater than that in the Z direction. For instance, the maximum velocity of the L1AR3 lining fragment in the X direction is 1.97 times that of the corresponding value in the Z direction. Moreover, during the initial motion phase of the lining fragments, as the fragments are close to the tunnel wall and farther from the train, their translational velocities are nearly zero. With the increase in time, the translational velocities of the fragments in both the X and Z directions tend to increase, accompanied by more significant fluctuations.
- (2) When the drop position of the lining fragments changes, the following patterns are observed: The average translational velocity in the X direction for both the L1AR3 and L5AR3 lining

fragments is significantly greater than that for the L2AR3, L3AR3, and L4AR3 fragments; the average translational velocity in the X direction for the L1AR3 lining fragment is 1.59 times that of the corresponding value for the L5AR3 fragment. For the L2AR3, L3AR3, and L4AR3 fragments, as the distance between the initial position of the fragment and the tunnel's centerline increases, the average velocities in both the X and Z directions decrease. Specifically, the average velocities in the X and Z directions for the L4AR3 fragment are only 30.9% and 36.2% of the corresponding values for the L2AR3 fragment, respectively.

- (3) When the AR of the lining fragments changes, the following patterns are observed: Under the condition of equal total mass, the average velocities of the lining fragments in both the X and Z directions increase with an increase in AR. When the AR increases from two to four, the average velocities in the X and Z directions for the lining fragments increase by 103.4% and 97.6%, respectively.

## 2. Falling debris rotation

Figures 17 and 18 present a comparison of the rotational angles and angular velocity time histories as the initial circumferential position and the AR of the lining fragments change. As depicted in Figs. 17 and 18:

- (1) Under conditions of different initial circumferential positions and various AR, the lining fragments predominantly rotate around the X and Z axes, with relatively smaller rotational angles around the Y axis. For instance, for the L1AR3 fragment, the maximum rotational angles around the X and Z axes reached up to  $783.4^\circ$  and  $-535.8^\circ$ , respectively, while the maximum rotational angle around the Y axis is less than  $90^\circ$  (only  $75.6^\circ$ ). In the latter half of the fragment's motion, a more

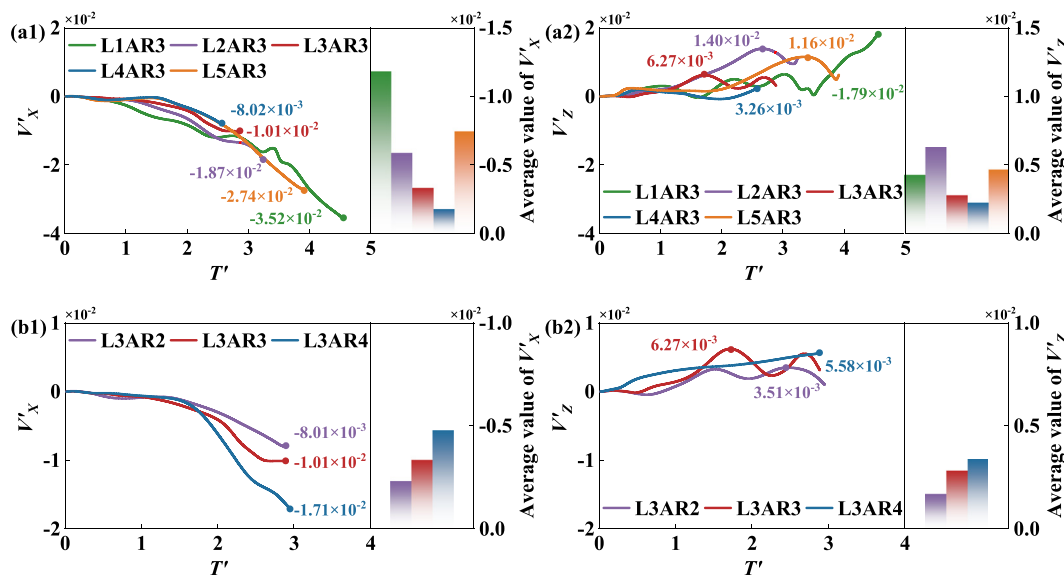


FIG. 16. Longitudinal and lateral translational velocities of the lining fragment: (a) different initial circumferential positions and (b) different AR.



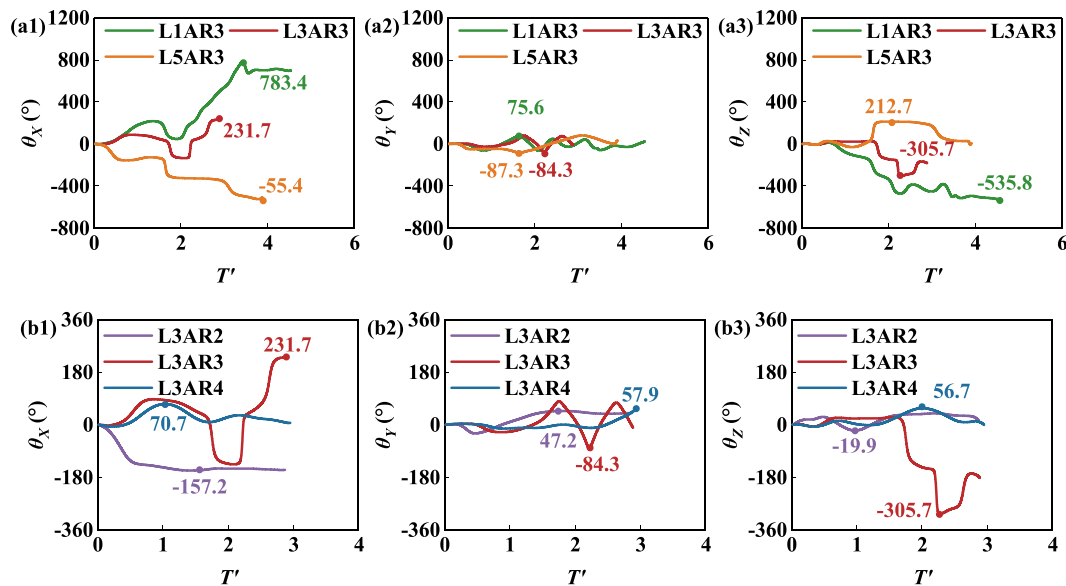


FIG. 17. Rotational angular time history curve of lining fragment: (a) different initial circumferential positions and (b) different AR.

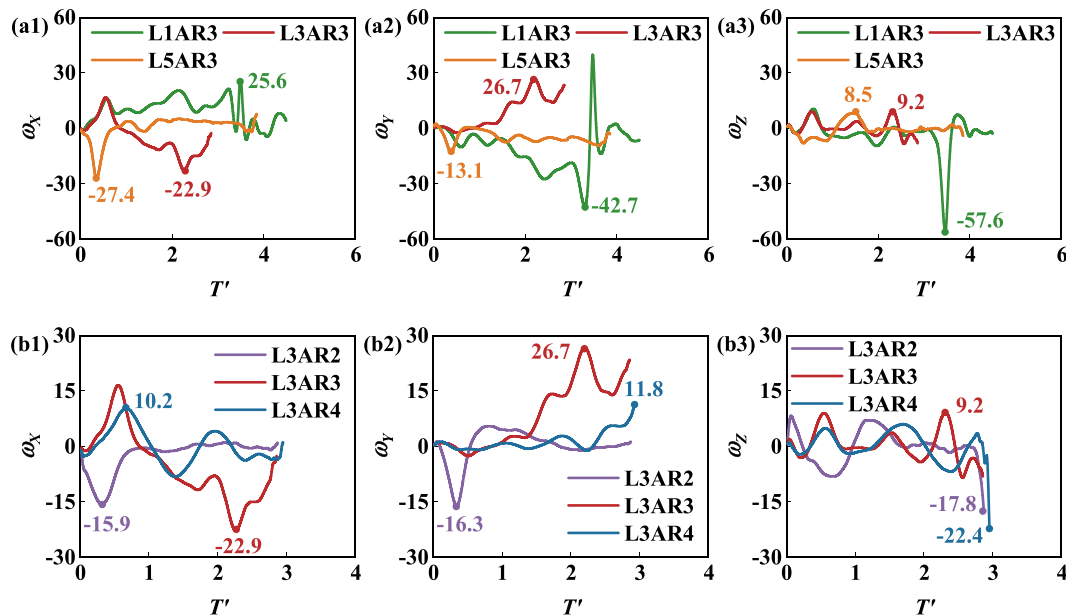


FIG. 18. Rotational angular velocity time history curve of lining fragment: (a) different initial circumferential positions and (b) different AR.

pronounced change in the angular velocity is observed compared to the first half, indicating that the train wind has a more significant impact on the rotation of the lining fragments in the latter stage. Nonetheless, in contrast to the regular rotational behavior of square fragments reported in previous studies,<sup>6,26</sup> the rotational angles and angular velocities of irregular-shaped lining fragments under the influence of train wind are more challenging to predict due to their irregularity.

(2) When the initial circumferential position of the lining fragments changes, the following patterns are observed: For the rotational angle around the X-axis, the L1AR3 fragment, located at the centerline of the track, consistently maintains a positive value, while the L5AR3 fragment, situated closer to the tunnel wall, consistently maintains a negative value. The L3AR3 fragment, located directly above the train, fluctuates around zero; for the rotational angle around the Z-axis, the

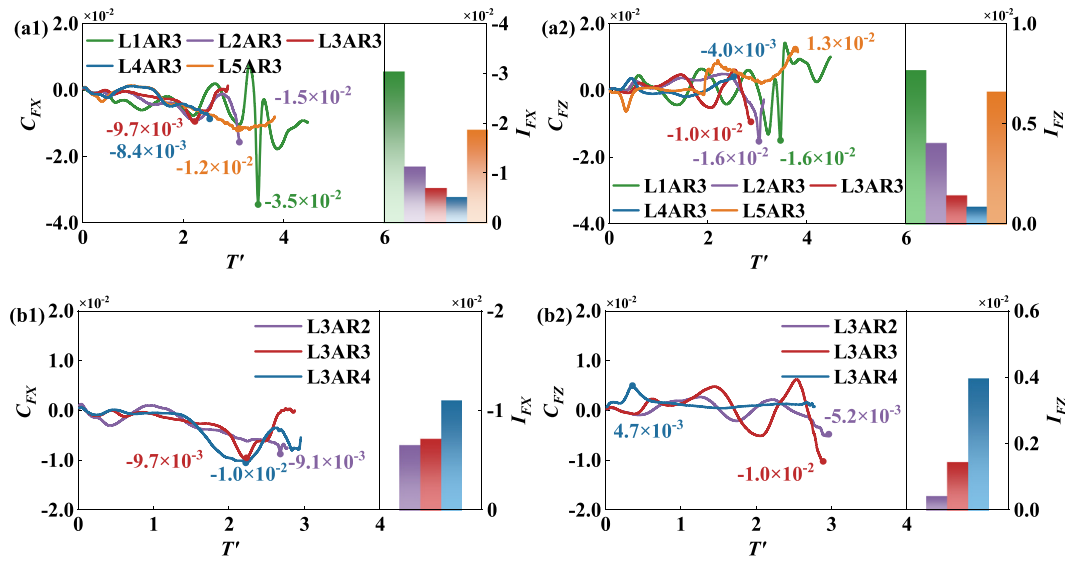


FIG. 19. Aerodynamic force coefficients time history curve of lining fragment: (a) different initial circumferential positions and (b) different AR.

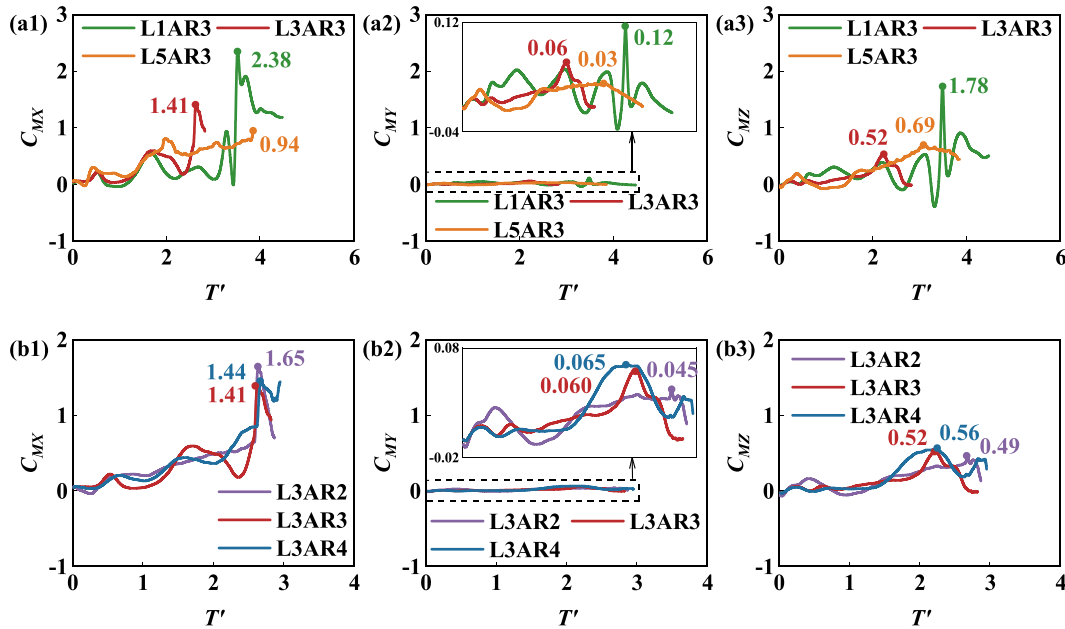


FIG. 20. Aerodynamic moment coefficients time history curve of lining fragment: (a) different initial circumferential positions and (b) different AR.

L3AR3 fragment also fluctuates around zero, but the patterns for the L1AR3 and L5AR3 fragments are opposite to those around the X-axis. The variation in the angular velocity of the L1AR3 fragment is greater than that of L3AR3 and L5AR3. For example, the maximum angular velocity of the L1AR3 fragment around the Z-axis reached  $-57.6$ , while the corresponding values for L3AR3 and L5AR3 fragments are only  $9.2$  and  $8.5$ , respectively.

(3) When the AR changes, the L3AR3 fragment exhibits the most significant changes in rotational angle and angular velocity, while the changes for L3AR4 fragment are the least pronounced. The pattern reflected in Fig. 17(b) differs from that in Fig. 14, indicating that there is no apparent correlation between the rotational angle and angular velocity and the AR. However, it is worth noting that among the three lining fragments with different AR, the mass distribution of the L3AR3 fragment is

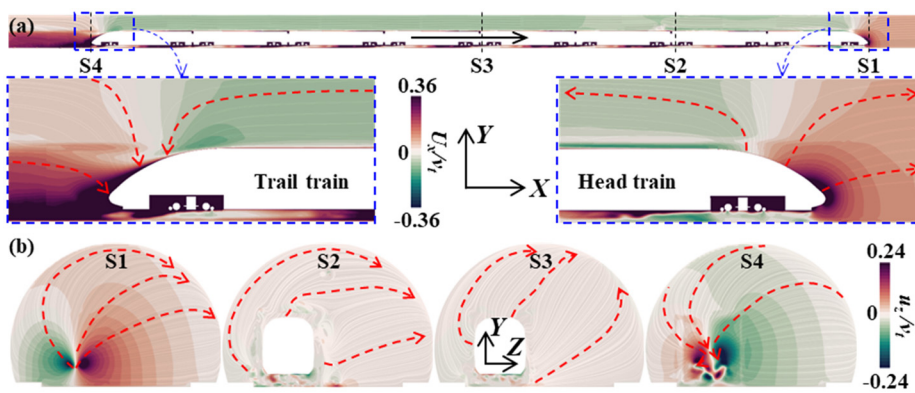


FIG. 21. Macroscopic flow field within the tunnel: (a) longitudinal section and (b) cross section.

the most uneven, while the mass distributions of L3AR2 and L3AR4 fragments are more uniform, as shown in Fig. 5. This may be the primary reason for the most pronounced rotational behavior of the L3AR3 fragment and warrants further

investigation in subsequent studies. These phenomena also demonstrate that using regular shapes to describe the rotational behavior of the originally irregular-shaped lining fragments is inadequate.

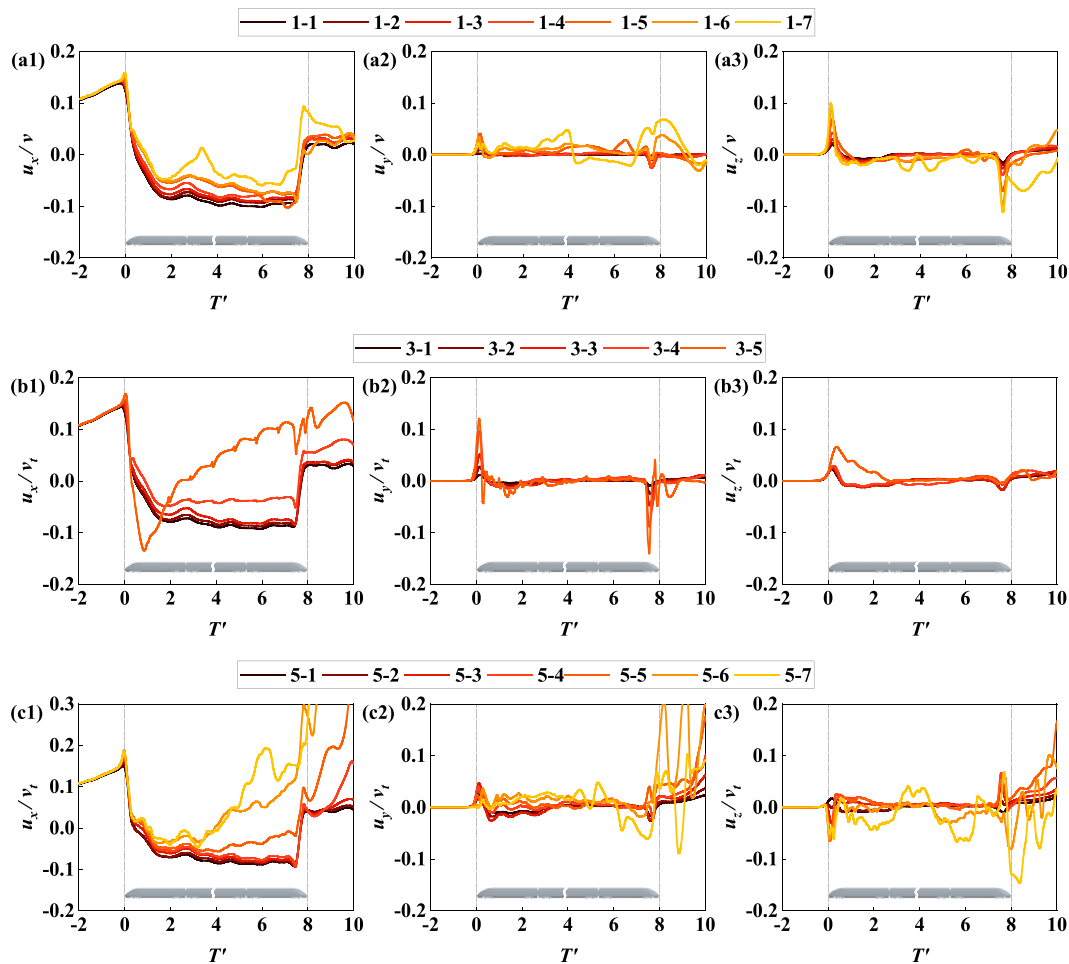


FIG. 22. Wind speed time history curve: (a) line 1; (b) line 2; and (c) line 3.

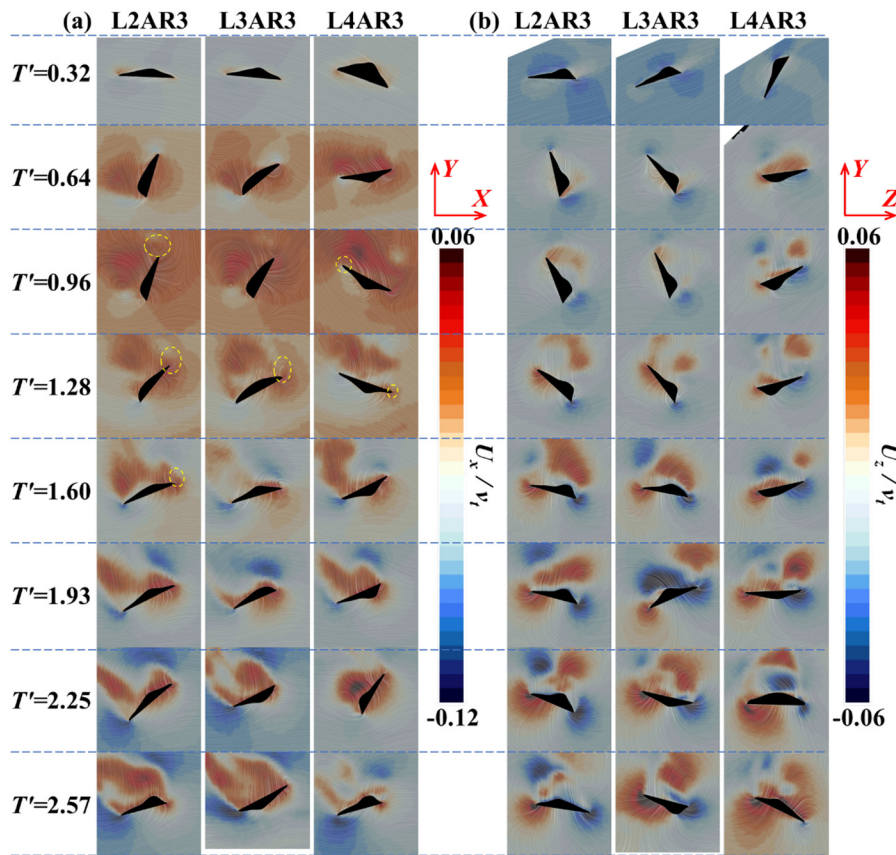


FIG. 23. Streamlines of wind speed around L2AR3, L3AR3, and L4AR3: (a) XY plane and (b) YZ plane.

## B. Aerodynamic characteristics of falling debris

Figure 19(a) compares the impact of the initial circumferential position on the time history of the aerodynamic force coefficients of the lining fragments, while Fig. 19(b) contrasts the influence of the AR of the lining fragments. Figure 19 also presents the magnitude of the impulse ( $I$ ) experienced by the lining fragments, which is the integral of the aerodynamic coefficients over time, used to describe the cumulative effect of aerodynamic forces on the motion of the lining fragments. As depicted in Fig. 19:

- (1) Under the action of train slipstream, the aerodynamic forces on the lining fragments exhibit continuous and irregular fluctuations. Lining fragments with different initial circumferential positions and various AR are all subjected to aerodynamic forces in the negative  $X$  direction, with the corresponding impulses being negative, causing the lining fragments to move in the negative  $X$  direction. The force coefficient in the  $Z$  direction ( $C_{FZ}$ ) fluctuates around zero, with the corresponding impulses being positive, causing the lining fragments to move in the positive  $Z$  direction.
- (2) When the initial circumferential position of the lining fragments changes, the following patterns are observed: The impulse values corresponding to the  $C_{FX}$  and  $C_{FZ}$  of the L1AR3 and L5AR3 fragments are significantly greater than those of the L2AR3, L3AR3, and L4AR3 fragments; the impulse values corresponding to the  $C_{FX}$  and  $C_{FZ}$  of the L1AR3 fragment are 1.62

and 1.16 times those of the corresponding values for L5AR3 fragment, respectively. For the L2AR3, L3AR3, and L4AR3 fragments, as the distance between the lining fragment and the tunnel's centerline increases, the impulse values corresponding to the  $C_{FX}$  and  $C_{FZ}$  decrease. Specifically, the impulse values corresponding to the  $C_{FX}$  and  $C_{FZ}$  of the L4AR3 fragment are only 46.8% and 21.7% of the corresponding values for L2AR3 fragment, respectively. This is the main reason for the decrease in both the longitudinal and lateral translational distances of the three lining fragments.

- (3) When the AR of the lining fragments changes, the following patterns are observed: Under the condition of equal total mass, the impulse values corresponding to the  $C_{FX}$  and  $C_{FZ}$  of the lining fragments increase with the increase in AR. When the AR increases from two to four, the impulse values corresponding to the  $C_{FX}$  and  $C_{FZ}$  of the lining fragments increase by 68.5% and 811.4%, respectively. This is the main reason for the decrease in both the longitudinal and lateral translational distances of the lining fragments with the increase in AR.

Figure 20 presents the impact of the lining fragment's initial circumferential position and AR on the time history of the aerodynamic moment coefficients of the lining fragment. As depicted in Fig. 20:

The moment coefficients of the lining fragment exhibit similarity to its rotational behavior, that is, the moment coefficients are relatively



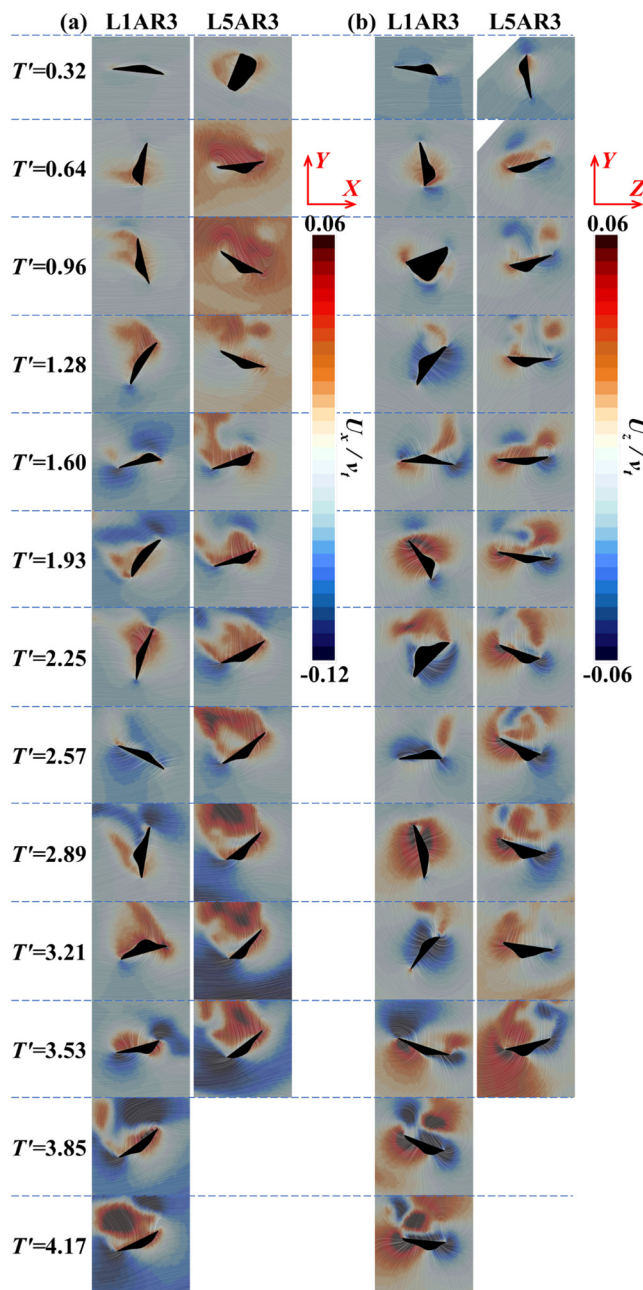


FIG. 24. Streamlines of wind speed around L1AR3 and L5AR3: (a) XY plane and (b) YZ plane.

stable, while the variations in the latter half are more pronounced than in the first half, leading to irregular rotational behavior of the lining fragment. When the initial circumferential position and AR of the lining fragment change, the moment coefficient around the X-axis ( $C_{MX}$ ) consistently remains the largest among the three aerodynamic moment coefficients, and the moment coefficient around the Y-axis ( $C_{MY}$ ) is significantly smaller than  $C_{MX}$  and  $C_{MZ}$ . For example, the

positive peak values of  $C_{MX}$  and  $C_{MZ}$  for the L1AR3 fragment reached 2.38 and 1.78, respectively, while the positive peak value of  $C_{MY}$  was only 0.12. This is the reason why the rotation of the lining fragment around the Y-axis is the least pronounced.

## C. Evolution mechanism of flow field

### 1. Macroscopic flow field in the tunnel

The macroscopic flow field within the tunnel aids in understanding the general characteristics of the motion behavior of lining fragments. Taking the moment when the train's nose reaches the center cross section of the tunnel as an example, Fig. 21 presents the macroscopic flow field diagram within the tunnel, with the longitudinal and transverse wind speed components ( $u_x/v_t$  and  $u_z/v_t$ ) are used to color the longitudinal and transverse diagrams, respectively, where  $v_t$  represents the train's velocity.

As shown in Fig. 21, the operation of the train induces complex and intense changes in the flow field within the tunnel. Longitudinally, two regions of high-speed airflow can be observed near the front and rear of the train. The movement of the train compresses the air in front of the nose and causes it to flow forward, forming a high-velocity wind area at the nose. At the same time, due to the pressure gradient present at the nose and tail of the train, the air above the train body primarily flows backward, which is the macroscopic flow field mechanism for the backward motion of lining fragments in the X direction. Near the rear of the train, a high-velocity wind area is formed as the air flows into the space previously occupied by the train. The airflow behind the tail exhibits a more complex flow pattern. Transversely, in cross section S1, the wind speed is highest near the nose and gradually decreases vertically and horizontally. Observing cross section S2 and S3, it can be seen that the air surrounding the train primarily flows in the positive Z direction, a flow characteristic that results in the motion of lining fragments toward the positive Z direction.

Figure 22 presents the wind speed time history curves of the three components of train wind ( $u_x$ ,  $u_y$ , and  $u_z$ ) during the train's passage through the tunnel, with the moment the train arrives at the center cross section of the tunnel defined as time zero for convenience. As shown in Fig. 22:

- (1) The train wind generated during the train's operation within the tunnel exhibits significant three-dimensional effects, causing the lining fragment to undergo three-dimensional motion. The most intense changes in train wind occur when the train's nose and tail pass by. Among the three components of train wind,  $u_x$  is significantly larger than  $u_y$  and  $u_z$ , and  $u_y$  has the smallest value among them; hence, the translation of the lining fragment in the X direction is the most pronounced. Before the train's nose reaches the cross section where the virtual probes are located,  $u_x$  is positive, then it becomes negative and remains a relatively stable negative value. After the tail of the train passes the cross section where the virtual probes are located,  $u_x$  fluctuates rapidly and returns to near zero. For  $u_y$  and  $u_z$ , both components only show significant changes when the nose and tail of the train pass, with the rest of the time remaining essentially stable at zero.
- (2) Observing the wind speed time history curves corresponding to virtual probes on line 1, line 3, and line 5, it is noted that the

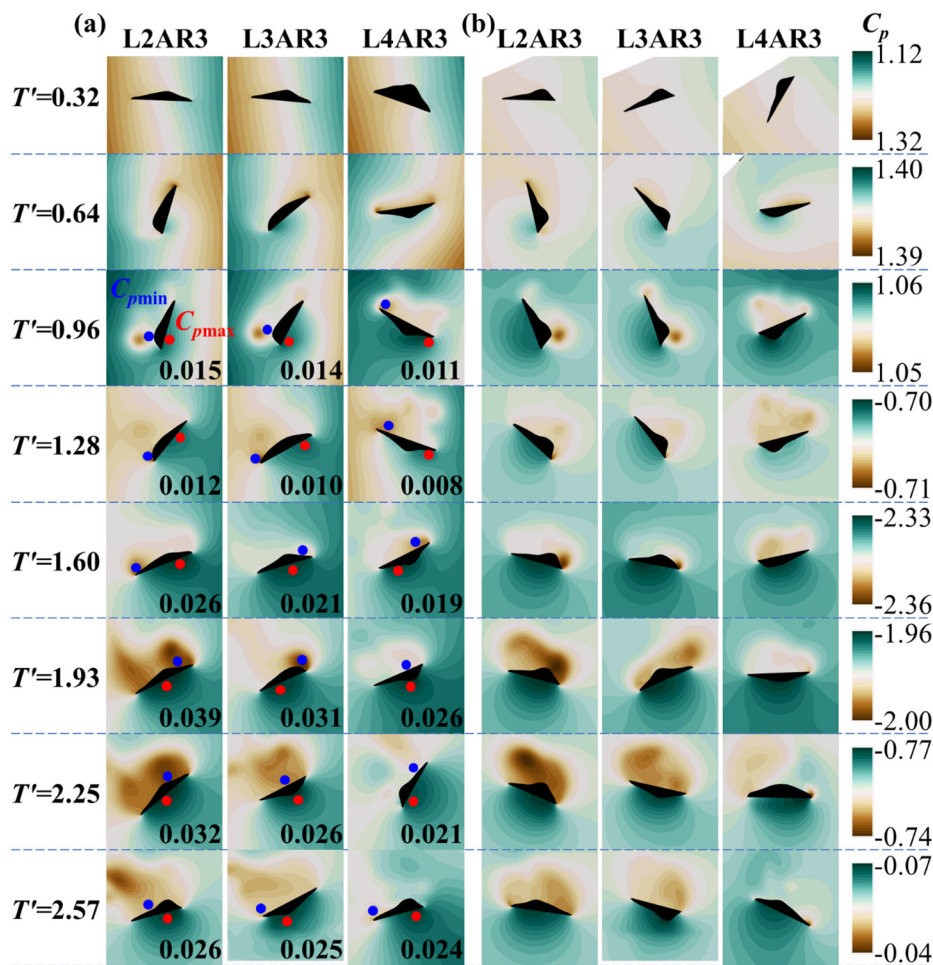


FIG. 25. Pressure contour around L2AR3, L3AR3, and L4AR3: (a) XY plane and (b) YZ plane.

closer the position to the train's surface or the tunnel's floor, the greater the fluctuation in the wind speed time history curve, indicating more intense turbulence. This is the macroscopic reason for the more pronounced fluctuations in the translational velocity and rotational angles of the lining fragment in the latter half stage compared to the first half stage. Comparing line 1, line 3, and line 5, the wind speed fluctuations on line 5 are more severe, which is due to the narrow space between the train and the tunnel wall leading to the most intense turbulence.

## 2. Flow field around the falling debris with different initial position

To elucidate the differential mechanisms underlying the motion characteristics of lining fragments under different initial positions, Fig. 23 presents local streamline diagrams near L2AR3, L3AR3 fragments, and L4AR3 at various times, colored by wind speed. Figure 24, on the other hand, provides the wind speed contour plots for L1AR3 and L5AR3 fragments. From Figs. 22–24, it can be observed that:

- (1) Within the XY plane, due to the obstruction of the lining fragment to the airflow, flow separation occurs at the edges of the

- lining fragment, generating vortices of varying scales. The edges of the lining fragment located at the center of the vortex structures have lower wind speeds (white color in the contour plot), while other positions have higher wind speeds. Before  $T' = 1.28$ , the flow field of the cross section where the lining fragment is located is predominantly the positive X direction flow near the train's nose, with lower wind speeds at the edges of the lining fragment. After  $T' = 1.28$ , the flow field near the cross section where the lining fragment is located is mainly the negative X direction flow near the train's body, but both the flat and rough surfaces of the lining fragment are acted upon by the positive X direction airflow. Within the XY plane, the alternating positive and negative wind speeds near the lining fragment cause complex rotational motion of the lining fragment around the Y axis.
- (2) Within the YZ plane, the flow field near the cross section where the lining fragment is located is predominantly the positive Z direction flow near the train's nose, with the flow separation and circulation around the lining fragment being similarly complex. When the airflow passes the lining fragment in the positive Z direction, the windward edge of the lining fragment is primarily subjected to the positive Z direction wind speed, while the leeward edge is mainly subjected to the negative Z direction



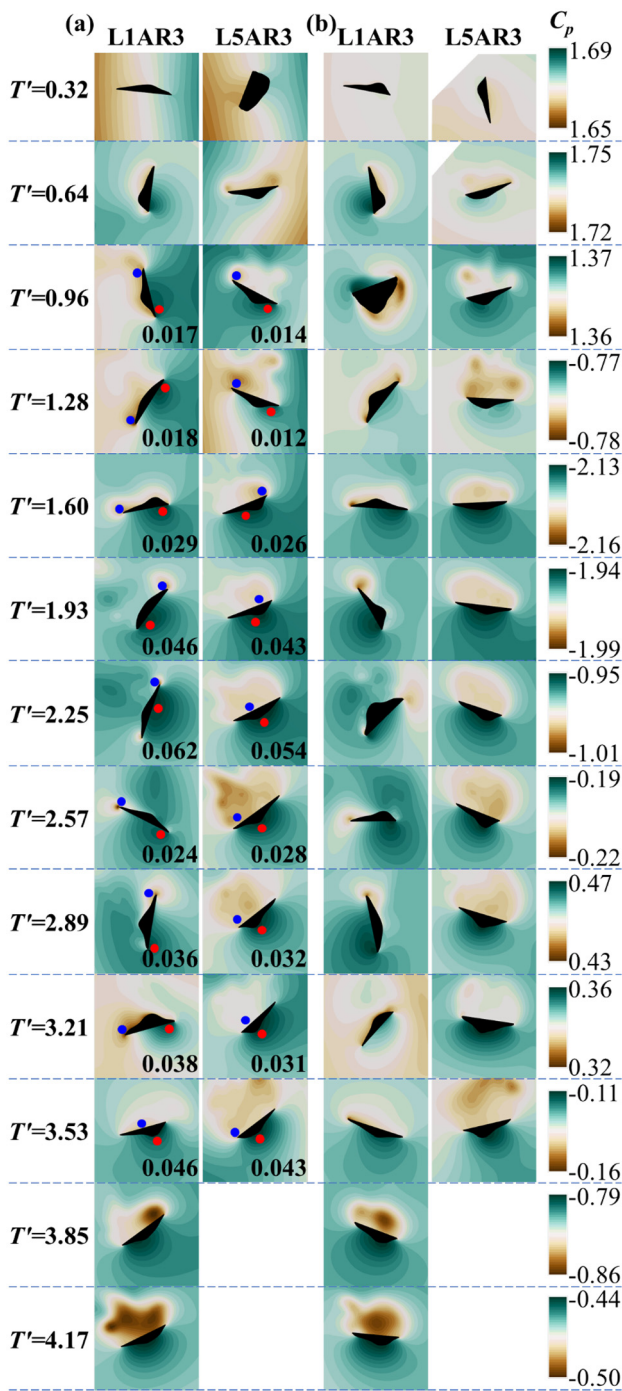


FIG. 26. Pressure contour around L1AR3 and L5AR3: (a) XY plane and (b) YZ plane.

wind speed. Within the YZ plane, the alternation of positive and negative wind speeds is more pronounced than in the XY plane. For example, in Fig. 23(b), from  $T' = 1.60$  to  $T' = 2.57$ , there is an alternating area of positive and negative wind speeds

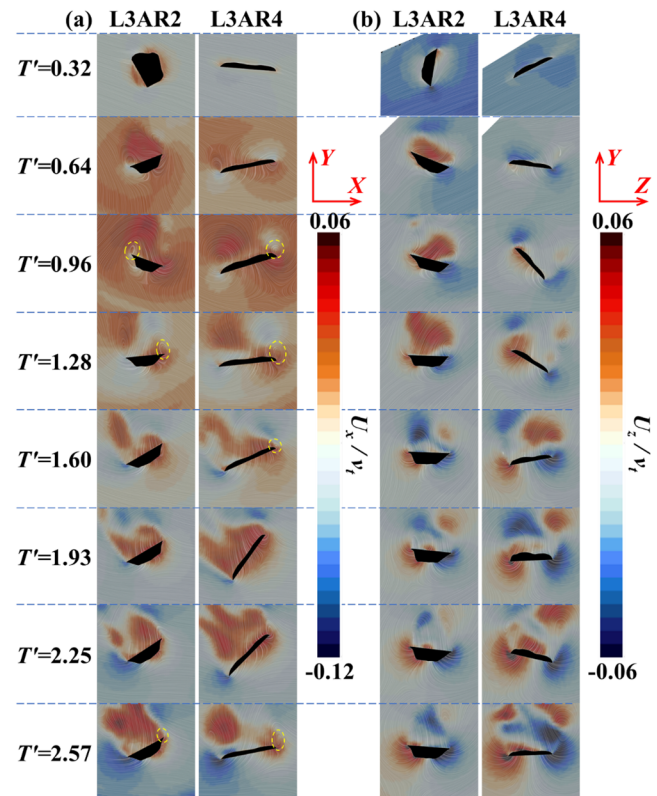


FIG. 27. Streamlines of wind speed around lining fragments with different AR: (a) XY plane and (b) YZ plane.

on the rough surface of the lining fragment. The combined effect of the alternating positive and negative wind speeds at the edges and on the rough surface of the lining fragment results in intense rotational motion of the lining fragment around the X-axis. A similar phenomenon can also be observed in Fig. 24(b).

Figure 25 presents the pressure contour plots near L2AR3, L3AR3, and L4AR3 fragments, while Fig. 26 provides the pressure contour plots for L1AR3 and L5AR3 fragments. For ease of observation, contour plots at different times adopt different upper and lower limits. Some plots also mark the locations of maximum and minimum pressures (red and blue dots, respectively), and the pressure coefficient difference between the two sides of the lining fragment is also given. As shown in Figs. 25 and 26:

- (1) Before  $T' = 0.96$ , the lining fragments are predominantly under the influence of positive pressure fields, and after  $T' = 0.96$ , they are mainly within negative pressure fields. This is because, between cross sections S1 and S2, the pressure near the tunnel wall is positive, while the pressure near the train body is negative (see Fig. 21). During the falling process of the lining fragments, the complex flow separation and circulation phenomena near the lining fragments result in uneven pressure differences acting on the flat and rough surfaces of the lining fragments. For instance, for L2AR3 and L3AR3 fragments, before

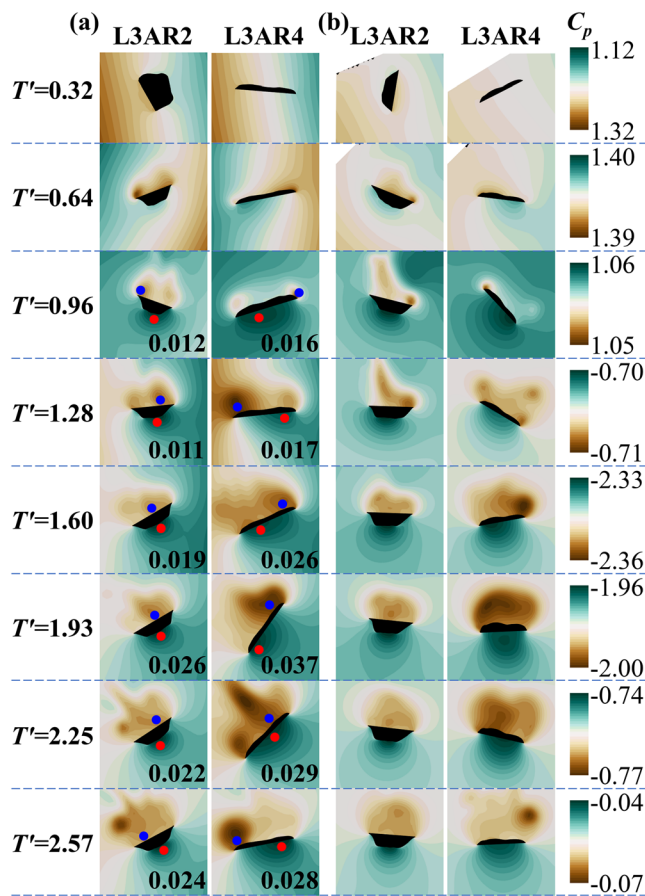


FIG. 28. Pressure contour around lining fragments with different AR: (a) XY plane and (b) YZ plane.

$T' = 0.96$ , the positive pressure on the rough surface is less than that on the flat surface; after  $T' = 0.96$ , the negative pressure on the rough surface is greater than that on the flat surface. Within the XY plane, before  $T' = 0.96$ , the positive X side of the lining fragment experiences a greater positive pressure, while after  $T' = 0.96$ , the negative X side experiences a greater negative pressure. These factors result in the lining fragments being subject to aerodynamic forces in the negative X direction throughout the falling process, leading to translational motion toward the negative X direction. Similar phenomena can also be observed within the YZ plane, causing the lining fragments to move in the positive Z direction.

- (2) For L2AR3, L3AR3, and L4AR3 fragments, as the distance between the initial circumferential position of the lining fragment and the tunnel's centerline increases, the pressure difference between the smooth and rough surfaces of the lining fragments gradually decreases. For example, at  $T' = 1.93$ , the pressure difference between the two surfaces of L2AR3 fragment reaches 0.39, which is 1.26 and 1.50 times that of L3AR3 and L4AR3 fragments, respectively. During the time interval from  $T' = 0.96$  to  $T' = 2.57$ , the average pressure difference between

the two surfaces of L2AR3 fragment is 1.18 and 1.38 times that of L3AR3 and L4AR3 fragments, respectively. These factors result in the displacement of the lining fragments in the X and Z directions decreasing as the distance between the initial circumferential position of the lining fragment and the tunnel's centerline increases. Similarly, at  $T' = 2.25$ , the pressure difference between the two surfaces of L1AR3 fragment is 1.15 times that of L5AR3 fragment. During the time interval from  $T' = 0.96$  to  $T' = 3.53$ , the average pressure difference between the two surfaces of L1AR3 fragment is 1.12 times that of L5AR3. It is worth noting that, in addition to flow field reasons, the initial Y-coordinate of the lining fragment also has a certain impact on the translational distance of the lining fragment. The greater the initial Y-coordinate of the lining fragment, the longer the falling time, and thus the further the translational distance.

### 3. Microscopic flow field around the falling debris with different AR

To further elucidate more microscopic differential mechanisms underlying the differences in the flight characteristics of lining fragments with varying AR, Fig. 27 presents the local streamline diagrams near L3AR2 and L3AR4 fragments at different times, while Fig. 28 provides the corresponding pressure contour plots. From Figs. 27 and 28, it can be observed that:

When the shape of the lining fragment changes, the flow separation and circulation phenomena occurring near the lining fragment are similar. The primary difference in the flow field near L3AR2 and L3AR4 fragments lies in the fact that the larger the AR value of the lining fragment, the larger the regions of positive and negative wind speeds on its surface, and the greater the pressure difference between the flat and rough surfaces. Specifically, at  $T' = 1.93$ , the pressure difference between the two surfaces of lining fragment L3AR4 reached 0.037, which is 1.42 times that of L3AR2. During the time interval from  $T' = 0.96$  to  $T' = 2.57$ , the average pressure difference between the two surfaces of L3AR4 fragment was 1.34 times that of L3AR2. This is the main reason for the increase in the translational distance of the lining fragment with the increase in AR.

Figure 29 presents the vorticity isosurface contour plots near lining fragments with different AR. Vorticity is used to describe the degree of rotation of the air. The greater the vorticity, the more intense the air rotation, indicating more severe turbulence. From Fig. 29, it can be more intuitively observed the complexity of turbulence in the three-dimensional space where the lining fragments are located when they fall within the train wind environment. At different stages of the lining fragment's fall, a ring-shaped vortex is attached to the edge of the lining fragment with different AR, confirming the presence of circulatory flow phenomena at the edges of the lining fragments, which is consistent with the phenomena reflected in the wind speed contour plots (Fig. 27). As time increases, the volume of the ring-shaped vortex at the edge of the lining fragment gradually increases, and vortex shedding phenomena gradually occur. After  $T' = 0.96$ , the vortex structures detached from the surface of the lining fragments exhibit significant random characteristics in terms of varying quantities and sizes, which is the main reason for the fluctuating rotational and translational behavior of the lining fragments over time. In addition, the vortex



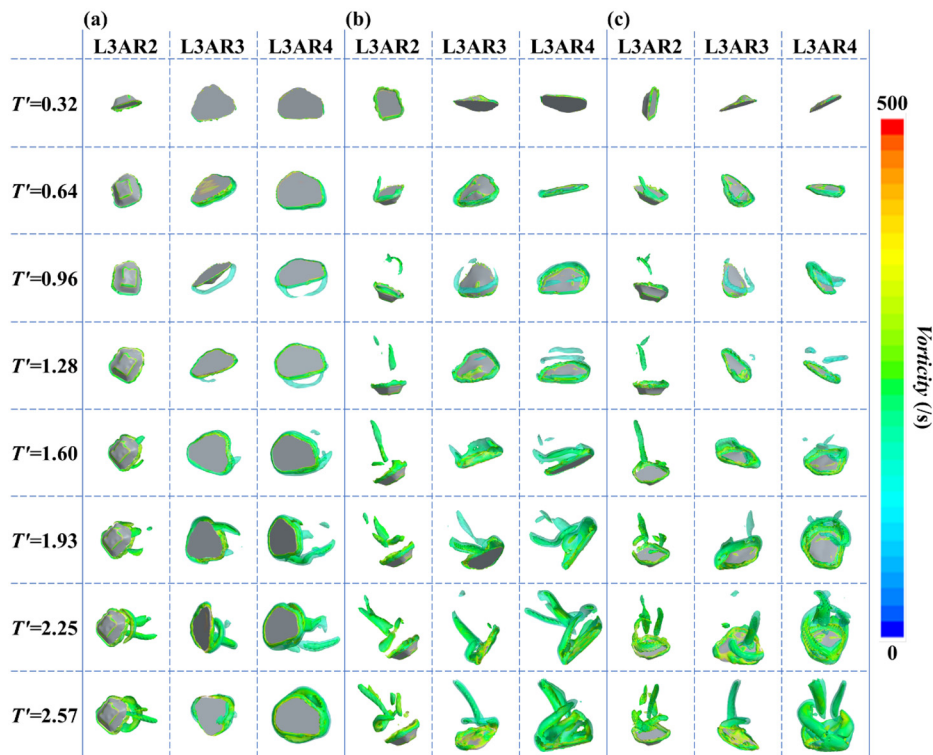


FIG. 29. Vortex structures near lining fragments of different AR: (a) XZ plane; (b) XY plane; and (c) YZ plane.

structures near the lining fragments increase with the increase in  $AR$ , which is the fundamental reason for the increase in pressure difference near the lining fragments with the increase in  $AR$ .

## VI. CONCLUSIONS

This study conducted an in-depth numerical simulation analysis of the aerodynamic behavior of lining fragments in high-speed railway tunnels. By on-site scanning method, irregular-shaped geometric numerical models of actual lining fragments are obtained, and the flight characteristics of lining fragments with different initial circumferential positions and shapes during high-speed train passage are simulated using the dynamic overset grid method. The accuracy of the numerical simulation method is verified by comparison with high-speed moving model experiments. The main conclusions are as follows:

- (1) The range of the aspect ratio ( $AR$ ) for the fragments is between two to seven, and the normalized lengths are between zero and 23. Among these samples, approximately 80% of the lining fragments have an  $AR$  value concentrated between two and four. The most representative lining fragments with an  $AR$  of three have a mass of 1.5 kg and are located 2.5 m from the tunnel centerline, with corresponding proportions of 17.6% and 10.8%.
- (2) Lining fragments exhibit three-dimensional motion characteristics under the action of train wind. The longitudinal translation distance of the fragments is significantly greater than the lateral translation distance, and the flight trajectory is in the opposite direction of the train's movement longitudinally and in the positive direction laterally. The rotational behavior of the lining

fragments is complex, primarily occurring around the longitudinal and lateral axes, with minimal rotation around the vertical axis.

- (3) There are significant differences in the translational patterns of lining fragments with different initial circumferential positions. The longitudinal and lateral movement distances of the tunnel centerline lining fragments are 45.3% and 5.2% less than those of the sidewall fragments. As the distance between the initial position of the lining fragment and the tunnel's centerline increases, the longitudinal and lateral translational distances of the top of the train lining fragments decrease, but all collide with the train's roof. As  $AR$  increases, the longitudinal and lateral flight distances and average velocities of the lining fragments increase. When the  $AR$  increases from two to four, the average velocities in the longitudinal and lateral directions increase by 103.4% and 97.6%.
- (4) The aerodynamic forces and moment coefficients acting on the lining fragments vary with the position and  $AR$  of the fragments. The tunnel vault and sidewall fragments experience greater lift and drag impulses than those on the train's roof. For the tunnel vault fragments, these impulses are 1.62 and 1.16 times the tunnel sidewall fragment's values. As the distance from the tunnel's centerline grows, these impulse values decrease. With an increase in  $AR$  from two to four, the impulses rise by 68.5% for lift and 811.4% for lift and drag.
- (5) The macroscopic flow field in the tunnel directly influences the motion of lining fragments. The train's operation produces high-speed airflow and pressure gradients that cause fragments to move backward longitudinally and forward laterally. The

longitudinal wind component is the strongest, with the vertical being the weakest, leading to more notable longitudinal movement of the fragments. Turbulence is heightened near the train's surface and tunnel floor, causing greater fluctuations in the fragments' velocity and rotation in the latter half of their path. The area between the train and the tunnel wall has the most intense turbulence.

- (6) The complex flow separation and circulation around lining fragments create uneven pressure on their surfaces, leading to irregular motion. The fragment at the top of the train closest to the tunnel centerline has average pressure differences of 1.18 and 1.38 times greater than the other two positions. The tunnel centerline fragment's pressure difference averages 1.12 times that of the sidewall fragment. Higher  $AR$  results in larger areas of positive and negative wind speeds and increased pressure differences between surfaces. A fragment with  $AR=4$  has 1.31 times the pressure difference of one with  $AR=2$ . Vortex structures near fragments grow with  $AR$ , explaining the increased pressure differences.

This study mainly focused on the impact of the initial circumferential position and geometric shape of the lining fragments on their aerodynamic performance. Future research could consider the coupled effects of more factors and develop a systematic risk assessment method and safety standards based on this.

## ACKNOWLEDGMENTS

This work is funded by the Science and Technology Research and Development Program Project of China Railway (Grant Number N2022G031), the Science and Technology Research and Development Program Project of China Railway Group Limited (Major Project No. 2021-Major-01), and the Science and Technology Research and Development Program Project of China Railway Group Limited (Major Project No. 2022-Key-23).

## AUTHOR DECLARATIONS

### Conflict of Interest

The authors have no conflicts to disclose.

### Author Contributions

**Hong He:** Conceptualization (lead); Investigation (lead); Software (lead); Writing – original draft (lead). **Wei-Chao Yang:** Funding acquisition (lead); Project administration (lead); Supervision (lead); Writing – review & editing (equal). **Yi-Kang Liu:** Data curation (lead); Supervision (equal); Writing – review & editing (lead). **E. Deng:** Funding acquisition (equal); Writing – review & editing (equal).

## DATA AVAILABILITY

The data that support the findings of this study are available from the corresponding author upon reasonable request.

## REFERENCES

- <sup>1</sup>C. Liu, D. L. Zhang, and S. L. Zhang, "Characteristics and treatment measures of lining damage: A case study on a mountain tunnel," *Eng. Fail. Anal.* **128**, 105595 (2021).
- <sup>2</sup>P. F. Li, Y. J. Wei, M. J. Zhang, Q. F. Huang, and F. Wang, "Influence of non-associated flow rule on passive face instability for shallow shield tunnels," *Tunn. Undergr. Space Technol.* **119**, 104202 (2022).
- <sup>3</sup>J. X. Chen, T. T. Hu, X. Hu, and K. Jia, "Study on the influence of crack depth on the safety of tunnel lining structure," *Tunn. Undergr. Space Technol.* **143**, 105470 (2024).
- <sup>4</sup>S. S. Xu, E. L. Ma, J. X. Lai, Y. T. Yang, H. T. Liu, C. P. Yang, and Q. Hu, "Diseases failures characteristics and countermeasures of expressway tunnel of water-rich strata: A case study," *Eng. Fail. Anal.* **134**, 106056 (2022).
- <sup>5</sup>T. Asakura and Y. Kojima, "Tunnel maintenance in Japan," *Tunn. Undergr. Space Technol.* **18**, 161–169 (2003).
- <sup>6</sup>C. H. Shi, A. Wang, X. H. Sun, and W. C. Yang, "Aerodynamic behavior and impact on driving safety of spalling blocks comprising high-speed-railway tunnel lining," *Appl. Sci. Basel* **12**, 2593 (2022).
- <sup>7</sup>J. D. Holmes, C. W. Letchford, and N. Lin, "Investigations of plate-type windborne debris—Part II: Computed trajectories," *J. Wind Eng. Ind. Aerodyn.* **94**, 21–39 (2006).
- <sup>8</sup>N. Lin, C. Letchford, and J. Holmes, "Investigation of plate-type windborne debris. Part I. Experiments in wind tunnel and full scale," *J. Wind Eng. Ind. Aerodyn.* **94**, 51–76 (2006).
- <sup>9</sup>A. Karimpour and N. B. Kaye, "On the stochastic nature of compact debris flight," *J. Wind Eng. Ind. Aerodyn.* **100**, 77–90 (2012).
- <sup>10</sup>V. Chai, D. Parkhi, S. Boopathy, J. T. Xiang, and J. Schlüter, "A model for the aerodynamic coefficients of rock-like debris," *C. R. Mecanique* **347**, 19–32 (2018).
- <sup>11</sup>F. Moghim and L. Caracoglia, "A numerical model for wind-borne compact debris trajectory estimation: Part 2—Simulated vertical gust effects on trajectory and mass momentum," *Eng. Struct.* **38**, 163–170 (2012).
- <sup>12</sup>F. Moghim and L. Caracoglia, "A numerical model for wind-borne compact debris trajectory estimation: Part 1—Probabilistic analysis of trajectory in the proximity of tall buildings," *Eng. Struct.* **38**, 153–162 (2012).
- <sup>13</sup>B. Kakimpa, D. M. Hargreaves, and J. S. Owen, "An investigation of plate-type windborne debris flight using coupled CFD-RBD models. Part I: Model development and validation," *J. Wind Eng. Ind. Aerodyn.* **111**, 95–103 (2012).
- <sup>14</sup>B. Kakimpa, D. M. Hargreaves, and J. S. Owen, "An investigation of plate-type windborne debris flight using coupled CFD-RBD models. Part II: Free and constrained flight," *J. Wind Eng. Ind. Aerodyn.* **111**, 104–116 (2012).
- <sup>15</sup>F. Xu, L. Yin, W. L. Chen, Z. D. Duan, and Y. Q. Xiao, "Numerical study on coupling flight characteristics of a plate-type windborne debris," *J. Wind Eng. Ind. Aerodyn.* **205**, 104319 (2020).
- <sup>16</sup>D. Saini and B. Shafei, "Flight characteristics of rod-shaped windborne debris objects in atmospheric boundary layer winds," *J. Wind Eng. Ind. Aerodyn.* **227**, 105073 (2022).
- <sup>17</sup>F. Bourriez, M. Sterling, and C. Baker, "Windborne debris trajectories in tornado-like flow field initiated from a low-rise building," *J. Wind Eng. Ind. Aerodyn.* **206**, 104358 (2020).
- <sup>18</sup>K. Uchibori and T. Tamura, "LES study on aerodynamics of auto-rotating square flat plate by IBM and SAMR," *J. Fluids Struct.* **89**, 108–122 (2019).
- <sup>19</sup>C. J. Baker and M. Sterling, "A conceptual model for wind and debris impact loading of structures due to tornadoes," *J. Wind Eng. Ind. Aerodyn.* **175**, 283–291 (2018).
- <sup>20</sup>T. Maruyama, "Simulation of flying debris using a numerically generated tornado-like vortex," *J. Wind Eng. Ind. Aerodyn.* **99**, 249–256 (2011).
- <sup>21</sup>Z. Q. Liu, Y. W. Cao, Y. Z. Wang, J. X. Cao, X. G. Hua, and S. Y. Cao, "Characteristics of compact debris induced by a tornado studied using large eddy simulations," *J. Wind Eng. Ind. Aerodyn.* **208**, 104422 (2021).
- <sup>22</sup>A. Premoli, D. Rocchi, P. Schito, C. Somaschini, and G. Tomasini, "Ballast flight under high-speed trains: Wind tunnel full-scale experimental tests," *J. Wind Eng. Ind. Aerodyn.* **145**, 351–361 (2015).
- <sup>23</sup>Y. Wang, T. T. Wang, C. Jiang, Y. D. Wu, C. L. Zhao, F. C. Shi, and X. D. Tian, "Numerical study on slipstream-induced snow drifting and accumulation in the bogie region of a high-speed train passing the snowy ballast bed," *J. Wind Eng. Ind. Aerodyn.* **232**, 105269 (2023).

- <sup>24</sup>A. Khayrullina, B. Blocken, W. Janssen, and J. Straathof, "CFD simulation of train aerodynamics: Train-induced wind conditions at an underground railroad passenger platform," *J. Wind Eng. Ind. Aerodyn.* **139**, 100–110 (2015).
- <sup>25</sup>C. H. Shi, A. Wang, X. H. Sun, and W. C. Yang, "Research on the movement law and traffic safety zoning of spalled blocks in the linings of high-speed railway tunnels," *Tunn. Undergr. Space Technol.* **128**, 104614 (2022).
- <sup>26</sup>W. C. Yang, J. B. Yang, E. Deng, Y. Q. Ni, and Y. K. Liu, "Aerodynamic behavior of flaky spalled blocks in high-speed rail tunnel lining under slipstream," *Tunn. Undergr. Space Technol.* **141**, 105377 (2023).
- <sup>27</sup>E. Deng, Y. K. Liu, W. C. Yang, and Y. Q. Ni, "Reproducing the flight behavior of falling debris from railway tunnel vault using a high-speed train ejection experiment and moving-overset-mesh simulation," *Tunn. Undergr. Space Technol.* **147**, 105670 (2024).
- <sup>28</sup>S. C. Fan, C. K. Lee, K. W. Kang, and Z. J. Wu, "Validation of a flight model for predicting debris trajectory from the explosion of an ammunition storage magazine," *J. Wind Eng. Ind. Aerodyn.* **136**, 114–126 (2015).
- <sup>29</sup>J. Wang, G. Minelli, T. Dong, G. Chen, and S. Krajnović, "The effect of bogie fairings on the slipstream and wake flow of a high-speed train. An IDDES study," *J. Wind Eng. Ind. Aerodyn.* **191**, 183–202 (2019).
- <sup>30</sup>Z. Guo, T. Liu, Z. Chen, Y. Xia, W. Li, and L. Li, "Aerodynamic influences of bogie's geometric complexity on high-speed trains under crosswind," *J. Wind Eng. Ind. Aerodyn.* **196**, 104053 (2020).
- <sup>31</sup>J. Wang, G. Minelli, T. Dong, K. He, and S. Krajnović, "Impact of the bogies and cavities on the aerodynamic behaviour of a high-speed train. An IDDES study," *J. Wind Eng. Ind. Aerodyn.* **207**, 104406 (2020).
- <sup>32</sup>Z. Dai, T. Li, W. Zhang, and J. Zhang, "Investigation on aerodynamic characteristics of high-speed trains with shields beneath bogies," *J. Wind Eng. Ind. Aerodyn.* **246**, 105666 (2024).
- <sup>33</sup>W. Wang, Y. Cao, and T. Okaze, "Comparison of hexahedral, tetrahedral and polyhedral cells for reproducing the wind field around an isolated building by LES," *Build. Environ.* **195**, 107717 (2021).
- <sup>34</sup>D. H. Ouyang, E. Deng, W. C. Yang, Y. Q. Ni, Z. W. Chen, Z. H. Zhu, and G. Y. Zhou, "Nonlinear aerodynamic loads and dynamic responses of high-speed trains passing each other in the tunnel-embankment section under crosswind," *Nonlinear Dyn.* **111**, 11989–12015 (2023).
- <sup>35</sup>H. Yue, J. Wang, E. Deng, Y. Q. Ni, W. C. Yang, X. Y. Liu, and C. M. Tsang, "How do crosswinds from two turbulent generators affect the aerodynamic loads of running trains at tunnel entrances?," *Phys. Fluids* **35**, 125137 (2023).
- <sup>36</sup>K. He, X. Su, G. Gao, and S. Krajnović, "Evaluation of LES, IDDES and URANS for prediction of flow around a streamlined high-speed train," *J. Wind Eng. Ind. Aerodyn.* **223**, 104952 (2022).
- <sup>37</sup>W. Yang, H. Yue, E. Deng, X. He, Y. Zou, and Y. Wang, "Comparison of aerodynamic performance of high-speed train driving on tunnel-bridge section under fluctuating winds based on three turbulence models," *J. Wind Eng. Ind. Aerodyn.* **228**, 105081 (2022).